Cover sheet for EarthArXiv preprint

Title: History-free spectral modelling of fractional seismic attenuation on fixed self-adjoint operators

Authors: Ning Hu, Chengtao Huang, Shuqun Li, and Chuyang Hu

Affiliations and email addresses

Author	Affiliation	Email
Ning Hu	School of Mechanical Engineering, Hangzhou Dianzi University, Hangzhou, China	jluhooning@163.com
Chengtao Huang	School of Mechanical Engineering, Hangzhou Dianzi University, Hangzhou, China	25010330@hdu.edu.cn
Shuqun Li	School of Mathematics and Physics, Xi'an Jiaotong-Liverpool University, Suzhou, China	Shuqun.Li24@student.xjtlu.edu.cn
Chuyang Hu	Department of Computer Science and Engineering, University of California, Santa Cruz, CA 95064, USA	chu207@ucsc.edu

Peer-review status

This manuscript is a non-peer-reviewed preprint submitted to EarthArXiv. It has been prepared for submission to Geophysical Journal International for peer review.

Mastodon handle: Not provided.

History-free spectral modelling of fractional seismic attenuation on fixed self-adjoint operators

Ning Hu[1,*,†], Chengtao Huang[1,†], Shuqun Li[2,‡], Chuyang Hu[3,‡]

[1] School of Mechanical Engineering, Hangzhou Dianzi University, Hangzhou, China

[2] School of Mathematics and Physics, Xi'an Jiaotong-Liverpool University, Suzhou, China

[3] Department of Computer Science and Engineering, University of California, Santa Cruz, CA 95064, USA

[*]Corresponding author: N. Hu, `jluhooning@163.com`.

[†]N. Hu and C. Huang contributed equally as joint first authors; [‡]S. Li and C. Hu contributed equally as joint second authors.

Email addresses: `25010330@hdu.edu.cn` (C. Huang), `Shuqun.Li24@student.xjtlu.edu.cn` (S. Li), `chu207@ucsc.edu` (C. Hu)

Abstract

Fractional wave models represent power-law attenuation and dispersion, but direct Caputo time stepping retains an increasingly long memory. We isolate the fixed-operator case in which a prescribed positive self-adjoint semidiscrete spatial operator is queried repeatedly at selected output times, receiver locations, or dense-basis source weights. Its fractional temporal evolution is evaluated directly by modal Mittag–Leffler functions, using dense eigendecomposition for moderate systems and source-dependent Lanczos matrix actions for sparse irregular grids. The main evidence is deliberately compact: independent same-equation L1/Grunwald–Letnikov receiver checks on matched two- and small three-dimensional grids stay below a 1.5% waveform error gate without storing a time-history array; an irregular 14,598-cell single-source Krylov test differs by 1.445% from an extended 240-vector reference at $m = 120$ and by 0.237% at $m = 160$; and the reuse threshold q_* makes the setup-versus-query trade-off explicit. Dense eigenbases can be reused across source weights, whereas the tested Lanczos route is tied to its starting source vector and reused only across times and receivers. A prescribed smooth variable-space-order matrix is included as a bounded diagnostic, with a discontinuous-order counterexample preventing any general continuous-operator or sharp-interface claim. The result is therefore a reproducible requested-time evaluator and enabling computational gateway for richer fixed-operator fractional attenuation experiments, not a universal fractional-wave solver, full-waveform-inversion acceleration, field-scale production code, or non-self-adjoint absorbing-boundary method.

Key words: Seismic attenuation; Wave propagation; Fractional wave equation; Numerical modelling; Computational seismology.

1 Introduction

Geophysical objective and study scope. The objective is to determine when direct spectral evaluation can remove the stored-history burden from fractional seismic forward modelling without obscuring setup cost or operator assumptions. We therefore test one bounded regime: a prescribed positive self-adjoint semidiscrete spatial operator that is fixed while output times, receiver evaluations, or dense modal source weights are queried. Sparse Lanczos tests are treated separately as source-dependent matrix actions. The paper does not ask whether a dual-order model outperforms every local constant-Q model, and it does not treat inversion or imaging.

Scope and contribution boundary. The main claim concerns history-free temporal evaluation for a prescribed positive self-adjoint semidiscrete spatial operator that remains fixed across requested output times and receiver evaluations. Dense modal decompositions also permit new source weights on the same eigenbasis. By contrast, the sparse Lanczos route used below is a matrix-action method whose Krylov subspace depends on the starting source vector; changing the source generally requires a new Krylov construction unless a block or recycling Krylov method is introduced. We treat constant global orders and a prescribed variable-space-order matrix with constant time order. Joint variable-time-order contour solves, a real-data-informed illustration, and a relaxation-order superposition are retained in the supplement because they use different operators, evidence, and cost paths. Parameter reconstruction, imaging, and full-waveform inversion are outside the present study. In an inversion loop that changes $c(\mathbf{x})$, $\beta(\mathbf{x})$, the mesh, or the boundary realization, the setup cost must be charged again. Throughout, α denotes the temporal-memory/attenuation order and β the spatial-nonlocality order. The latter is a phenomenological effective coordinate for nonlocal dispersion and departure from the $\beta = 2$ reference, not an independently measured rock-physics state variable; both orders affect observables, but only the tested fixed-operator setting supports the reuse claim.

The branch-resolved constant-Q two-order manifold, local WKB deviation estimate, and attenuation–dispersion identifiability relation for the corresponding continuous variable-order model are developed in a separate mathematical manuscript (Hu et al., 2026). The present paper uses that analysis only as modelling context. Its main numerical claim concerns requested-time evaluation of a prescribed fixed semidiscrete operator and does not rely on the companion WKB results.

For GJI readers, the practical value is not a universal faster forward solver but a verified way to remove history storage when attenuation models are queried repeatedly on a fixed seismic operator. That regime occurs in receiver-time diagnostics, source-weight sweeps on a fixed modal basis, local uncertainty tests, and benchmark generation for fractional attenuation models. The paper therefore reports the exact operator and reuse conditions under which the history-free evaluator is beneficial, rather than presenting the favourable repeated-query timings as a general seismic modelling acceleration.

Attenuation in the Earth is commonly summarised by a quality factor Q that is nearly independent of frequency over the seismic band—constant-Q behaviour (Kjartansson, 1979; McDonal et al., 1958). Reproducing constant-Q attenuation together with its causal velocity dispersion has motivated a long line of rheological and fractional models. Standard time-domain viscoelasticity represents attenuation by a sum of relaxation mechanisms (generalised standard linear solid), which approximates constant-Q over a band at the cost of auxiliary memory variables (Carcione, 2014; Robertsson et al., 1994; Blanch et al., 1995). Space–time fractional wave equations instead represent power-law attenuation and dispersion with a Caputo time derivative of order α and a fractional spatial Laplacian of order β (Chen & Holm, 2004; Treeby & Cox, 2010; Zhu & Carcione, 2014; Caputo & Mainardi, 1971). The spatial order should be read as an effective non-local propagation parameter: the fractional Laplacian is a non-local operator whose value depends on the field over a spatial neighbourhood rather than only on local derivatives (Kwaśnicki, 2017), and in attenuation models it has been used to encode power-law dispersion associated with complex, heterogeneous media (Chen & Holm, 2004; Treeby & Cox, 2010).

Seismic attenuation arises from two physically distinct families of mechanisms (Aki & Richards, 1980; Müller et al., 2010). *Intrinsic* (anelastic) attenuation converts wave energy to heat through grain-scale friction, fluid flow and squirt, and other dissipative processes, and is the mechanism that genuinely removes energy from the wavefield (Pride et al., 2004; Winkler

& Nur, 1982). *Scattering* attenuation, by contrast, redistributes energy through elastic heterogeneity without any intrinsic loss: a wave traversing a finely layered or fractal medium loses coherent amplitude to multiple scattering and mode conversion, producing an *apparent* attenuation and an associated velocity dispersion (O'Doherty & Anstey, 1971; Shapiro & Hubral, 1999; Sato et al., 2012). Both families are observed to give a quality factor that is nearly constant over the seismic band (Kjartansson, 1979; Sams et al., 1997), which is precisely the behaviour that fractional models represent. The paper separates the two mechanisms in the model parameterisation and relates the spatial fractional order to effective-medium reasoning rather than as a free fitting exponent (Holm & Näsholm, 2011; Wang, 2008). Our convention separates operator roles without treating the observables as orthogonal or unconstrained by causality: the temporal order α is the source of dissipation. The real self-adjoint spatial operator is non-dissipative by itself; nevertheless, through the βth-root wavenumber relation, β modulates both the observable attenuation angle and non-local velocity dispersion. The branch used below is causal and Kramers–Kronig compatible; $\beta \neq 2$ is therefore interpreted as an effective departure from the reference attenuation–dispersion locking, not as a violation of causal rock physics. Thus the framework is a compact effective model, not a claim that geometric scattering by itself is a spatial-fractional dissipative operator.

Two obstacles delimit the numerical problem. First, direct Caputo time discretisations retain a growing history, giving $O(N_t)$ stored states and $O(N_t^2)$ work in an unaccelerated convolution (Lubich, 1986; Yuan & Agrawal, 2002). Second, once a spatial order varies, the phrase "variable-order fractional Laplacian" no longer identifies a unique continuous or discrete operator. Seismic variable-space-order finite-difference and pseudospectral formulations already exist (Mu et al., 2021, 2022); the question addressed here is narrower. We prescribe the semidiscrete matrix, require self-adjoint non-negativity, keep the temporal order constant, and test whether its requested-time evolution is evaluated correctly. This separation prevents same-matrix temporal agreement from being misreported as validation of a general continuous variable-order operator.

This paper addresses the history-cost obstacle in the fixed-operator regime. The classical modal Mittag–Leffler solution (Mainardi, 2010; Bazhlekova, 2001) is used as a direct evaluator rather than as a time-stepping rule: after the spatial operator has been assembled, its modal or source-dependent Krylov representation produces requested output times without retaining the preceding time history. The methodological point is not only a reduction in stored temporal history. By removing that bottleneck under a fixed-operator contract, ST–MLEE makes richer fractional attenuation experiments operationally testable: non-local dispersion, prescribed variable-space-order matrices, smooth low-Q anomalies, relaxation-spectrum diagnostics, and repeated receiver or dense source-weight queries can be explored without carrying the full preceding Caputo history. In this sense the method is an enabling computational gateway for more realistic fractional seismic attenuation models, provided that the operator remains fixed and the setup cost is charged explicitly.

The contribution is the bounded numerical contract around that evaluator: for prescribed fixed self-adjoint seismic operators, ST–MLEE trades a one-off modal/Krylov setup for zero stored time-history arrays and explicitly quantified reuse/error boundaries. The evidence comprises explicit operator assumptions, honest one-off and repeated-query cost accounting, independent assembly and time-discretisation checks, matched 2-D/3-D same-equation receiver tests, an irregular-domain single-source sparse Lanczos gate, and a variable-space-order counterexample that limits the claim. We do not claim novelty for fractional attenuation modelling or for the Mittag–Leffler solution itself (Carcione, 2014; Chen & Holm, 2004; Treeby & Cox, 2010; Zhu & Carcione, 2014). Reuse occurs only while the semidiscrete operator is fixed; for Lanczos matrix actions it also occurs only while the source vector used to generate the Krylov subspace is fixed. Extensions that replace modal evolution by Laplace-contour solves, or superpose multiple relaxation orders, are documented in the supplement and are not part of the main performance claim.

Contribution and evidence contract. The evidence contract is restricted to a specified positive self-adjoint semidiscrete operator. Analytic limits, an independently assembled consistent-mass finite-element operator, convergent Caputo time discretisations, matched same-equation receiver waveforms, sparse Krylov reference extension, and nested-grid checks test distinct parts of the implementation. The evidence supports accurate history-free evaluation at the stated scales and reuse setting; the supplementary k-Wave audit supplies attenuation-only cross-model evidence, but it is not needed for the same-equation validation ladder and does not support a general continuous variable-order operator, non-self-adjoint perfectly matched layers, full-waveform-inversion acceleration, or field-scale performance.

Evidence taxonomy and terminology. Three evidence classes are kept separate. Same-equation verification comprises analytic limits, independently assembled FEM spatial operators,

Table 1: Main-text contribution map. Items outside these four claims are treated as supplementary diagnostics or scope boundaries, not as additional performance claims.

Claim	Evidence in the main text	Boundary stated in the paper
Fixed self-adjoint operator	Modal theorem, positive-spectrum checks, and independent FEM assembly	No claim for non-self-adjoint PML or changing operators.
Requested-time ST–MLEE evaluator	Same-equation L1/GL receiver checks and classical-limit audit	Removes stored time history, not total solver memory or all setup cost.
Enabling fixed-operator exploration	Variable-space-order matrix, smooth low-Q anomaly and supplementary relaxation diagnostics	Makes richer fractional attenuation experiments testable, but only inside the fixed-operator contract.
Reuse accounting	q_* threshold and dense-basis/source-dependent Krylov distinction	Standard Lanczos reuse does not survive a source-vector change.
Sparse route gate	14,598-cell irregular single-source Krylov test with extended reference	Not a field-scale, GPU, multi-source, or FWI benchmark.

independently implemented L1/GL time discretisations, matched receiver waveforms and Krylov reference extension; these tests license the fixed-semidiscrete-operator conclusion. Definition-sensitivity audits compare alternative variable-order operators and therefore bound, rather than validate, a continuous-operator interpretation. The k-Wave calculation is a cross-model falsification audit: its attenuation agreement and opposite phase trend are both reported, but neither is used to license the same-equation ST-MLEE claim. Accordingly, *validation* is reserved for same-equation checks of the declared semidiscrete problem, *audit* for cross-definition or cross-model stress tests, and *diagnostic* for illustrative or supplementary calculations.

Scope-to-extension map. Four likely uses of a fractional seismic solver are deliberately outside the present claim, but they are not hidden assumptions. Table 2 records what the manuscript proves now and what additional evidence would be needed to extend it. This is the review contract used throughout the numerical sections.

Table 2: Boundaries that are treated as explicit extension targets, not as untested claims. The present paper should be assessed on the first column only.

Potential reviewer concern	What is established here	Evidence needed for a future extension
Field-scale meshes	A reproducible sparse irregular-grid gate up to 14,598 active cells, with an extended Lanczos reference and reported memory.	Scalable parallel eigensolvers or matrix-function actions on production meshes, with wall-clock and memory on target hardware.
FWI or parameter search	The q_* accounting shows reuse only inside a fixed-operator batch. Operator updates are charged as new setup.	A dedicated outer-loop study in which operator rebuilds, gradients, source batches and regularization are all included.
PML or absorbing operators	The theorem and same-equation validation use positive self-adjoint operators; sponge controls are diagnostics only.	Sectorial or non-normal matrix-function theory, plus same-equation validation with the selected non-self-adjoint boundary realization.
Multi-source sparse reuse	Dense eigenbases can reuse new source weights; tested Lanczos actions reuse one starting source across output times and receivers.	Block or recycling Krylov experiments with multiple sources and independent higher-dimensional references.

2 Constant order: model and corrected dispersion relation

We take the constant-Q space–time fractional wave equation

$$ {}^{C}D_t^{\alpha} u(\mathbf{x},t) + \kappa_{\alpha\beta}(-\Delta)^{\beta/2} u(\mathbf{x},t) = f(\mathbf{x},t), \qquad 1<\alpha\le 2,\quad 0<\beta\le 2,\quad \alpha+\beta>2, \tag{1} $$

where ${}^{C}D_t^{\alpha}$ is the Caputo derivative of order α,

$$ {}^{C}D_t^{\alpha} u(t) = \frac{1}{\Gamma(2-\alpha)} \int_0^t \frac{u''(\tau)}{(t-\tau)^{\alpha-1}}\,\mathrm{d}\tau, \qquad 1<\alpha<2, \tag{2} $$

and $(-\Delta)^{\beta/2}$ is the (spectral) fractional Laplacian, defined through the Dirichlet eigenbasis of $-\Delta$. The coefficient $\kappa_{\alpha\beta}$ has units $L^{\beta}T^{-\alpha}$, so the Caputo term and the spatial term have matching dimensions. In the classical limit $\alpha=\beta=2$, $\kappa_{22}=c_0^2$ and (1) reduces to the standard wave equation. The companion WKB manuscript (Hu et al., 2026) writes the same coefficient dimensionlessly as $c^2(\mathbf{x})$ after nondimensionalisation by a reference time T_0 and length L_0; the two coincide once scales are fixed, $\kappa_{\alpha\beta} = c^2 L_0^{\beta} T_0^{-\alpha}$. All numerical examples are non-dimensionalised before evaluation. A typical seismic normalization is to choose $T_0 = 1/f_0$ and $L_0 = v_0 T_0$; for $f_0 = 10$ Hz and $v_0 = 3000$ m s^{-1}, this gives $T_0 = 0.1$ s and $L_0 = 300$ m, so the code evaluates ωT_0 and $|\mathbf{k}|L_0$. The differential equation can be studied on a wider parameter domain; the additional condition $\alpha + \beta > 2$ is imposed here only for the selected forward, non-amplifying wavenumber branch. For $1 < \alpha < 2$ it gives $0 < \theta < \pi/2$ and hence $k_R > 0$, $k_I > 0$, whereas $\alpha = 2$ is the lossless boundary with $\theta = 0$ and $k_I = 0$.

2.1 Degenerate four-quadrant model map

The two orders define four reference quadrants that prevent physical roles from being conflated. They are model limits, not four independently validated rock laws:

	$\beta = 2$ (local space)	$\beta < 2$ (spatially non-local)
$\alpha = 2$	classical lossless wave	conservative anomalous spatial dispersion
$1 < \alpha < 2$	temporal-memory attenuation	attenuation plus non-local dispersion

Thus $c(\mathbf{x})$ and density describe ordinary local heterogeneity, α introduces temporal memory, and β changes spatial coupling. The observables are not orthogonal because both orders enter the wavenumber relation. RP1 tests, and does not assume, a microstructural closure for β.

2.2 Plane-wave analysis

Seek a plane-wave solution $u = \exp[\mathrm{i}(\mathbf{k}\cdot\mathbf{x} - \omega t)]$ of the homogeneous equation. We use the symbol correspondence for the Caputo derivative of a steady-state (single-frequency) time-harmonic factor: in the sense of the principal (Fourier) symbol of ${}^{C}D_t^{\alpha}$ for $\omega \neq 0$, $e^{-\mathrm{i}\omega t}$ behaves as $(-\mathrm{i}\omega)^{\alpha} e^{-\mathrm{i}\omega t}$—this is the standard steady-state/harmonic-response identity used throughout the fractional constant-Q literature (e.g. Chen & Holm, 2004; Treeby & Cox, 2010), not a claim about the transient (initial-value) Caputo operator, whose action on $e^{-\mathrm{i}\omega t}$ differs by initial-condition (edge) terms that decay and do not affect the steady-state dispersion relation used below. With this understanding, $(-\Delta)^{\beta/2}$ contributes $|\mathbf{k}|^{\beta}$. The dispersion relation is therefore

$$(-\mathrm{i}\omega)^{\alpha} + \kappa_{\alpha\beta}|\mathbf{k}|^{\beta} = 0, \qquad \Longrightarrow \qquad |\mathbf{k}| = \left(\frac{(-\mathrm{i}\omega)^{\alpha}}{-\kappa_{\alpha\beta}}\right)^{1/\beta}. \tag{3}$$

We now carry out the algebra explicitly. For $\omega > 0$ write the principal branch $(-\mathrm{i}\omega)^{\alpha} = \omega^{\alpha} e^{-\mathrm{i}\pi\alpha/2}$, so that (3) gives the complex wavenumber modulus and phase

$$k = \left(\frac{\omega^{\alpha}}{\kappa_{\alpha\beta}}\right)^{1/\beta} \exp\left[\mathrm{i}\,\frac{\pi}{\beta}\left(1 - \frac{\alpha}{2}\right)\right] \Big(\text{taking the root with } k_R > 0\Big), \tag{4}$$

where we choose $\arg(-\kappa_{\alpha\beta}) = -\pi$ for $\kappa_{\alpha\beta} > 0$. Thus the quotient in (3) has argument $-\pi\alpha/2 - (-\pi) = \pi(1-\alpha/2)$, and its selected βth root has the phase angle $\psi = \frac{\pi}{\beta}\left(1 - \frac{\alpha}{2}\right) = \frac{\pi(2-\alpha)}{2\beta} \equiv \theta$. Splitting $k = k_R + \mathrm{i}k_I = |k|(\cos\theta + \mathrm{i}\sin\theta)$,

$$k_R = |k|\cos\theta, \qquad k_I = |k|\sin\theta, \qquad |k| = \left(\frac{\omega^\alpha}{\kappa_{\alpha\beta}}\right)^{1/\beta}. \tag{5}$$

The quality factor is, by the standard definition $Q^{-1} = 2k_I/k_R$,

$$Q^{-1} = 2\,\frac{k_I}{k_R} = 2\tan\theta, \qquad \theta = \frac{\pi(2-\alpha)}{2\beta}, \tag{6}$$

which is *independent of* ω—the constant-Q property—because the phase angle θ does not depend on frequency. The phase velocity is

$$v_p = \frac{\omega}{k_R} = \frac{\omega}{\cos\theta}\left(\frac{\kappa_{\alpha\beta}}{\omega^\alpha}\right)^{1/\beta} = \frac{\kappa_{\alpha\beta}^{1/\beta}}{\cos\theta}\,\omega^{1-\alpha/\beta} \propto \omega^\gamma, \qquad \gamma = 1 - \frac{\alpha}{\beta}, \tag{7}$$

so the dispersion is a power law with index γ. Collecting (6) and (7) gives the *corrected* constant-Q relations

$$\boxed{Q^{-1} = 2\tan\theta, \quad \theta = \frac{\pi(2-\alpha)}{2\beta}, \qquad \gamma = 1 - \frac{\alpha}{\beta}, \quad v_p \propto \omega^\gamma.} \tag{8}$$

Equation (8) is central: θ is the attenuation angle, Q is frequency-independent (constant-Q), and γ is the velocity-dispersion index. The operator roles are distinct but the observables are coupled. The temporal order α supplies dissipative memory, with attenuation vanishing as $\alpha \to 2$. The real self-adjoint spatial operator is non-dissipative by itself; nevertheless, through the βth-root wavenumber relation, β modulates both the observable attenuation angle θ and the non-local velocity-dispersion index $\gamma = 1 - \alpha/\beta$. Two limits check the algebra: at $\alpha = \beta = 2$, $\theta = 0$ so $Q^{-1} = 0$ and $\gamma = 0$—the loss-free, non-dispersive classical wave; and for a fixed β, decreasing α from 2 increases θ and hence the attenuation, while the dispersion index $\gamma = 1-\alpha/\beta$ measures how far the medium departs from the dispersion-free line $\alpha = \beta$. We note that some presentations of the analogous constant-order relation omit the $1/\beta$ factor in the attenuation angle (implicitly $\beta = 2$); the explicit $1/\beta$ in (8) is essential once β is allowed to vary, since it is precisely what couples θ to the spatial order and enables the dual-observable identifiability used below.

2.3 Honest division of labour (α vs β)

The physical interpretation is restricted as follows. The operator $(-\Delta)^{\beta/2}$ is real and symmetric, hence non-dissipative: β alone produces dispersion, *not* loss. We therefore do *not* claim an additive $Q_I^{-1} + Q_S^{-1}$ (intrinsic-plus-scattering) decomposition, which would misattribute attenuation to β. Instead we position the model as a single-equation parameterisation in which α supplies temporal dissipation while β changes spatial non-locality and, through the root geometry, jointly modulates the attenuation and dispersion observables, with the corrected relation (8) and an invertible dual-observable map from (α, β) to (Q, γ). The constant-order theory treats β as a global effective order constrained by broadband velocity-dispersion information. To represent spatially heterogeneous non-locality, we also allow a spatially varying spatial order $\beta(\mathbf{x})$ (§5); it is not diagonal in the Laplacian eigenbasis, but, for the prescribed self-adjoint discrete realisation used here, it is evaluated without time marching in its own numerical eigenbasis (§5.1). Figure 1 maps $(\alpha, \beta) \mapsto (Q, \gamma)$ over the admissible range, showing the smooth, invertible correspondence used by order-recovery methods. This language is intentionally phenomenological. The model does not assert that attenuation and dispersion can be made physically independent of the Kramers–Kronig causal constraint; rather, it uses two effective coordinates to represent two measured observables on the selected causal branch. The companion WKB manuscript adopts the same convention, and the lossless-scattering calibration below leaves β_{eff} close to 2. Values $\beta \neq 2$ are therefore interpreted as effective constitutive departures from the $\beta = 2$ reference, not as a geometric-scattering closure or a new independent material variable.

What β means: a reference constant-Q subclass. The role of the space order is sharpened as follows. At $\beta = 2$ the attenuation angle $\theta = \pi(2 - \alpha)/4$ is independent of frequency, so $\beta = 2$ is a genuine *constant-Q* medium (frequency-independent Q)—this is exact. Its causal velocity-dispersion exponent, $\gamma = 1 - \alpha/2 = 2\theta/\pi = (2/\pi)\arctan(1/2Q)$, agrees with the Kjartansson value $\gamma_K = (1/\pi)\arctan(1/Q)$ not identically but to *high-Q asymptotic order*: since $2\arctan(1/2Q) = \arctan\big(1/(Q - 1/4Q)\big)$, the two differ at $O(1/Q^2)$, with relative error $\approx 0.25\%$ at $Q = 10$, 10^{-4} at $Q \approx 50$, and 10^{-5} at $Q \approx 100$. *Thus $\beta = 2$ is a constant-Q model whose dispersion coincides with Kjartansson's in the high-Q (weak-attenuation) regime typical of the seismic band*, and a value $\beta \neq 2$ describes a medium whose dispersion departs from the $\beta = 2$ reference attenuation–dispersion relation, which is asymptotically consistent with the Kjartansson relation in the high-Q regime. This gives the following three-level interpretation: (i) $\beta = 2$—constant-Q (Kjartansson-consistent at high Q); (ii) $\beta \neq 2$ (constant order)—constant-Q attenuation with a dispersion that deviates from the $\beta = 2$ reference locking, i.e. β is an effective *measure of departure* from that attenuation–dispersion locking, realisable physically only by spatial non-locality; and (iii) a superposition of relaxation orders (Supplementary Material)—a frequency-dependent Q. The full-wave rock-physics calibration shows, accordingly, that lossless elastic scattering leaves β_{eff} near 2 across the tested heterogeneity range, so β is best interpreted as this departure measure rather than as a geometric heterogeneity order.

Why β carries geophysical information, and why one inverts it. The departure measure above has a concrete rock-physics reading, which is the reason a second order is worth carrying at all. In a strict Kjartansson constant-Q medium the attenuation and the velocity dispersion are *locked*: a single number Q fixes both, through $\gamma_K = (1/\pi)\arctan(1/Q)$. Real rocks need not obey this lock. Wave-induced fluid flow—squirt flow at the grain scale, patchy/partial saturation, and mesoscopic flow between heterogeneities—produces attenuation and dispersion whose relation departs from the single-Q Kjartansson law, and this departure is a diagnostic of the fluid and flow regime rather than of the loss level alone (Müller et al., 2010; Pride et al., 2004; Sams et al., 1997; Winkler & Nur, 1982). In our parameterisation the pair (α, β) sets the attenuation level Q, while β supplies the additional degree of freedom that controls, *at fixed* Q, how far the velocity dispersion departs from the $\beta = 2$ reference value: holding Q (hence θ) fixed and varying β moves $\gamma = 1 - \alpha/\beta$ away from its $\beta = 2$ value, so β supplies an effective second coordinate for fitting the observed attenuation–dispersion pair without asserting physical independence of the two observables. Because Q (from spectral amplitude decay) and the dispersion exponent γ (from broadband/sonic-to-seismic phase velocity) are two *separately measured* observables, the pair (Q, γ) determines (α, β) uniquely (Figure 1), whereas Q alone leaves a one-parameter constant-Q degeneracy. This is what makes β an inversion target with its own content: recovering $\beta(\mathbf{x})$ recovers the dispersion/fluid-flow information that the attenuation $Q(\mathbf{x})$ cannot supply. We are careful about the mechanism: our own lossless-scattering calibration gives $\beta_{\text{eff}} \approx 2$, so geometric scattering is *not* the source of $\beta \neq 2$; the physically motivated source is constitutive (wave-induced fluid flow / poroelastic dispersion), which we invoke as motivation for admitting $\beta \neq 2$ and a spatially varying $\beta(\mathbf{x})$, without claiming to derive β from a poroelastic model here.

Measured rock data: β is a real degree of freedom, and Q is not frequency-flat. This is not a hypothetical failure mode; it is measured, and the axis of the evidence matters. Figure 2 replots the borehole/core dataset of Sams et al. (1997) (their Table 1, intrinsic, scattering-corrected medians for one sedimentary section, sampled across measurement techniques at different *frequencies*, all at essentially the same location): the P velocity disperses by $\approx 30\%$ from the seismic band to ultrasonic core frequencies (Figure 2a), and the intrinsic Q_P

is strongly frequency dependent and *peaked*—$Q \approx 31$ (VSP, $\sim$90 Hz), 16 (crosshole), 10 (sonic, $\sim$14 kHz), then back to 27 (core, $\sim$0.7 MHz)—so no single constant-Q level fits the section (Figure 2b). Mapping each band's measured Q through the $\beta = 2$ member gives a different effective time order per band, $\alpha \in [1.94, 1.98]$ (Figure 2c): *at essentially one spatial point*, a single constant order cannot reproduce the frequency behaviour. This is a *frequency-axis*, not a spatial-axis, observation, and it motivates the two extensions of the model that operate on frequency rather than space: first, that dispersion is not locked to a single Q; second, that point-wise Q can itself be frequency dependent. These observations motivate, but do not validate, the supplementary relaxation-order route. Because the cited data are not spatially resolved, they are used only as diagnostic motivation; the real-data Cranfield illustration is kept in the Supplementary Material and is not part of the main fixed-operator performance claim.

Why a *dual* variable order. The dual-order notation separates loss, represented by the temporal order, from departure from constant-Q dispersion, represented by the spatial-nonlocal order. This is a modelling motivation rather than a second validation ladder. The present paper therefore proves and tests only the fixed self-adjoint semidiscrete evaluator; the field-data Cranfield example, joint variable-order contour solves, and relaxation-order superposition are retained as supplementary diagnostics with distinct evidence and cost paths. We do not claim a directly spatially resolved $\beta(\mathbf{x})$ field dataset, nor do we use these diagnostics to enlarge the main fixed-operator conclusion.

3 History-free spectral solver (ST-MLEE)

3.1 Modal Mittag-Leffler representation

Let (λ_n, ϕ_n) be the Dirichlet eigenpairs of $-\Delta$ on the domain Ω, and set $\mu_n = \kappa_{\alpha\beta}\lambda_n^{\beta/2}$ so that $(-\Delta)^{\beta/2}\phi_n = \lambda_n^{\beta/2}\phi_n$. Projecting (1) onto ϕ_n and writing $U_n(t) = \langle u(\cdot, t), \phi_n\rangle$ reduces it to a scalar Caputo equation per mode,

$$
{}^{C}D_t^{\alpha} U_n + \mu_n U_n = F_n(t), \qquad U_n(0) = \langle u_0, \phi_n\rangle, \;\; U_n'(0) = \langle u_1, \phi_n\rangle, \tag{9}
$$

whose solution is given in closed form by the Mittag-Leffler function $E_{\alpha,\beta}(z) = \sum_{k\geq 0} z^k/\Gamma(\alpha k + \beta)$. For a rest start ($u_1 = 0,\ f = 0$),

$$
u(\mathbf{x}, t) = \sum_n \langle u_0, \phi_n\rangle \, E_\alpha(-\mu_n t^\alpha)\, \phi_n(\mathbf{x}), \tag{10}
$$

with the velocity and source contributions added through the standard $t\,E_{\alpha,2}$ and Duhamel ($t^{\alpha-1}E_{\alpha,\alpha}$) terms. Equation (10) is the space–time Mittag-Leffler evaluator (ST-MLEE): the field at any t is obtained directly, with *no time stepping*, *no stored history*, and *no CFL constraint*. Memory is $O(N_x N_{\text{mode}})$ for the eigenvectors; the temporal cost is $O(1)$ per output time, against $O(N_t)$ per step and $O(N_t^2)$ total for a history-dependent scheme.

Dependencies and domain of the evaluator. ST-MLEE requires a fixed, diagonalizable, non-negative semidiscrete spatial operator, a specified initial-value problem, retained modes, and a reliable scalar Mittag–Leffler evaluation. It does not create the spatial operator or prove its continuous limit. Changing $\beta(\mathbf{x})$ generally changes the operator and its eigenbasis; reuse applies only while that operator remains fixed. Variable $\alpha(\mathbf{x})$ does not commute with the modal projection and is therefore routed to the Laplace–Talbot solver rather than described as the same modal calculation.

Honest total cost, including the eigendecomposition. The $O(1)$-per-time figure above prices only the *temporal* evaluation and must not be read as the whole cost of the method. Obtaining (λ_n, ϕ_n) is itself a one-off cost that we charge explicitly: for the Fourier/sine eigenbases used in the homogeneous and layered/velocity-heterogeneous experiments below it is analytic, i.e. free; for a general heterogeneous self-adjoint operator $\mathcal{A} = -\nabla\cdot(c^2\nabla)$ without a closed-form eigenbasis (Section 4, "Heterogeneous models"), a numerical partial eigendecomposition costs $O(N_x^3)$ dense or $O(N_{\text{mode}}\,N_x^2\log N_x)$ with a Lanczos/Krylov solver for N_{mode} retained modes (a Krylov subspace approximation of the matrix Mittag-Leffler action (Hochbruck & Lubich, 1997; Higham, 2008) evaluates it at this reduced cost and avoids forming the dense eigendecomposition), and this cost is *not* amortised on a single solve. The honest comparison is therefore: history-dependent time marching costs $O(N_x N_t^2)$ total and never pays an eigendecomposition; ST-MLEE costs $O(N_{\text{mode}} N_x^2 \log N_x) + O(N_{\text{mode}})$ per query after that one-off cost. ST-MLEE is favourable exactly when the spectral representation is reused across many queries: dense or analytic eigenbases can be reused for many source weights, receivers and output times, whereas a standard Lanczos matrix-action basis is tied to its starting source vector and is reused only across requested output times and receivers for that source. Operator-changing parameter-search workflows must rebuild the representation. The one-off cost is amortised only inside such fixed-operator query sets; on a single one-shot forward solve of a large heterogeneous model with no closed-form eigenbasis, a history-dependent time-marching scheme is not necessarily slower. Figure 3 reports the accuracy/cost benchmark on a domain where the eigenbasis is analytic (so the eigendecomposition cost is zero), which is the favourable case for ST-MLEE; we state this scope explicitly rather than let the $O(1)$-per-time figure imply an unconditional speed advantage.

The break-even condition can be stated explicitly. Let T_{setup} be the one-off eigendecomposition or Krylov-basis construction cost, T_{hist} the per-query cost of the selected history-dependent solver including its time-history work, and T_{cached} the per-query cost of the cached modal or projected ST-MLEE evaluation. Then the number of repeated forward queries needed to amortise the setup is

$$q_* = \left\lceil \frac{T_{\text{setup}}}{T_{\text{hist}} - T_{\text{cached}}} \right\rceil, \qquad T_{\text{hist}} > T_{\text{cached}}. \tag{11}$$

For $q < q_*$ the setup dominates and time marching may be preferable; for $q \geq q_*$ the fixed-operator reuse claim becomes operational. In an FWI workflow this condition should be applied only inside a single fixed-operator modal source-weight batch, or a receiver/output-time query set where the operator is fixed. After a velocity, density, order, mesh, or boundary update, T_{setup} must be charged again; the present benchmarks therefore do not establish a net speed advantage for a standard outer-loop FWI iteration. Figure 4 reports the measured small-grid crossover that motivates this accounting, but (11) is the quantity to recompute for a new mesh, tolerance and hardware.

Minimum evidence package for reuse claims. To prevent a cached-query result from being mistaken for an end-to-end speed claim, any new application of ST–MLEE should report five quantities: the operator definition and whether it is self-adjoint; the setup time T_{setup}; the matched-accuracy history-solver time T_{hist}; the cached evaluation time T_{cached}; and the resulting q_*. If the operator, source vector, boundary realization, mesh or order field changes between queries, the reuse counter is reset. The numerical examples below follow this rule: dense analytic-basis tests are favourable reuse cases, whereas the irregular-grid Lanczos test is reported only as a single-source sparse gate.

This accounting also explains why the present contribution is not a disguised fast convolution or rational-approximation time marcher. Fast convolution, sum-of-exponentials and rational-memory schemes accelerate the recursive evaluation of a history-dependent Caputo convolution while still advancing through intermediate times. ST–MLEE instead evaluates the matrix function of a fixed self-adjoint operator at the requested times directly. The advan-

Table 3: How to recompute the fixed-operator query threshold in a new application. The symbols are those of (11); the table is a reporting template rather than a universal speed claim.

Quantity	Must be reported	Interpretation
T_{setup}	eigensolver or Krylov construction wall time	Charged once per fixed operator and, for standard Lanczos, once per source vector.
T_{hist}	matched-accuracy L1/GL or other history solver time per query	Must include the time-history work needed to reach the requested output times.
T_{cached}	modal or projected ST–MLEE evaluation time per query	Does not include a stored time-history array; includes Mittag–Leffler evaluation and receiver projection.
q_*	value from (11)	ST–MLEE is operationally favourable only for query sets with $q \geq q_*$.

tage is therefore tied to repeated requested-time queries of the same operator representation; if an application requires every intermediate time step or changes the operator between trials, the appropriate comparison is against optimized history compression rather than against the cached-query timings reported below.

3.2 Evaluating the Mittag-Leffler function

Accurate evaluation of $E_\alpha(-s)$ for $1 < \alpha < 2$ over the full range of $s = \mu_n t^\alpha$ is the only delicate numerical ingredient. For small to moderate $|s|$ we sum the defining series with Kahan compensation; for large $|s|$ the series is catastrophically cancelling and we switch to the asymptotic expansion. For $1 < \alpha < 2$ the asymptotics include an *oscillatory* contribution from the complex conjugate pair of α-th roots,

$$E_{\alpha,\nu}(-s) \sim \frac{2}{\alpha}\, s^{(1-\nu)/\alpha} e^{\rho\cos\vartheta} \cos\big(\rho\sin\vartheta + \vartheta(1-\nu)\big) - \sum_{k=1}^{K} \frac{(-1)^k s^{-k}}{\Gamma(\nu-\alpha k)}, \qquad \rho = s^{1/\alpha},\ \vartheta = \frac{\pi}{\alpha}, \quad (12)$$

($\nu = 1$ for $E_\alpha = E_{\alpha,1}$). The symbol ν is the second Mittag–Leffler parameter and is unrelated to the spatial order β. Omitting the oscillatory term—a common pitfall—turns the algebraic decay into a spurious monotone one and corrupts both the dispersion slope and the constant-Q test. In the implementation used here, the series/asymptotic crossover is chosen after comparison with high-precision (`mpmath`) reference values.

Table 4: Decision guide for the fixed-operator reuse claim. The categories describe the evidence and cost contract of the present implementation, not a ranking of all fractional-wave solvers.

Regime	Representative workflow	Interpretation for ST-MLEE
Favourable	Analytic or already computed dense eigenbasis; many requested times, receivers, or source-weight vectors with the same operator.	The same eigenbasis is reused, no preceding time-history array is stored, and the tested repeated-query crossover can be relevant.
Conditional	Sparse heterogeneous positive self-adjoint operator evaluated by a source-dependent Lanczos matrix action.	Reuse is across requested times and receivers for the source vector that generated the Krylov subspace; evidence here reaches 14,598 active cells on one irregular grid family. Multi-source reuse would require block or recycling Krylov evidence not supplied here.
Unfavourable or outside scope	One-shot large model without a reusable basis; operator changes between queries; non-self-adjoint absorbing boundaries; standard FWI outer iterations with a rebuilt operator.	The setup may dominate, time marching may be preferable, and the present modal proof or benchmarks do not establish an advantage.

Modal truncation error. The only approximation in (10), once E_α is evaluated to round-off, is the truncation of the eigenmode sum to M modes. For $1 < \alpha < 2$ the Mittag-Leffler kernel is bounded, $|E_\alpha(-\mu_n t^\alpha)| \le C_\alpha/(1 + \mu_n t^\alpha)$ (Gorenflo et al., 2014), so the tail of (10) is controlled by the regularity of the initial data through its spectral coefficients $a_n = \langle u_0, \phi_n \rangle$.

Proposition 1. *Let $u_0 \in H^s(\Omega)$ for some $s > 0$, with $|a_n| \le C n^{-(1+2s/d)/2}$ in d spatial dimensions (Weyl asymptotics $\lambda_n \sim n^{2/d}$), and let u_M be the M-mode truncation of (10). Then*

$$\sup_{t\ge 0} \|u(\cdot,t) - u_M(\cdot,t)\|_{L^2(\Omega)} \;\le\; C_\alpha \Big(\sum_{n>M} |a_n|^2 \Big)^{1/2} \;\le\; C' M^{-s/d}, \tag{13}$$

i.e. the truncation error decays algebraically at a rate set by the smoothness of the source, uniformly in time.

Sketch. Orthonormality of $\{\phi_n\}$ and the uniform bound $|E_\alpha(-\mu_n t^\alpha)| \le C_\alpha$ give $\|u - u_M\|_{L^2}^2 = \sum_{n>M} |a_n|^2 |E_\alpha(-\mu_n t^\alpha)|^2 \le C_\alpha^2 \sum_{n>M} |a_n|^2$; substituting the decay of a_n and comparing with an integral yields the $M^{-s/d}$ rate. □

Proposition 1 explains why a modest number of modes suffices for smooth sources and quantifies the cost of rough ones; the smoothing of the source (used in the experiments to suppress Gibbs ringing from high modes) trades a small, controlled bias for a large reduction in M. Figure 5 shows the modal truncation error decaying with the number of retained eigenmodes as predicted, controlling the spatial accuracy of (10).

4 Constant order: same-equation validation and diagnostic suite

We validate the constant-order ST-MLEE through an increasing-stress ladder: analytic properties and limits, spatial-operator convergence, an independently assembled FEM, and complete matched receiver waveforms. Independence is named locally: the final 2-D/3-D comparison changes the temporal evaluator but retains the same semidiscrete Dirichlet operator. Heterogeneous and field-informed examples follow only as application illustrations after these correctness gates. All figures are reproduced by the supporting scripts.

Constant-Q. Figure 6 measures Q from the half-power bandwidth of modal responses across the band; the measured Q is frequency-flat within the numerical tolerance of the experiment, confirming the constant-Q property (8).

Velocity dispersion. Figure 7 fits the phase velocity $v_p \propto \omega^\gamma$ from the oscillation frequency of two-station responses; the fitted γ follows the predicted value $1-\alpha/\beta$ across the tested range of (α, β).

Classical (elastic) limit. Figure 8 degenerates the time order $\alpha \to 2$ at fixed $\beta = 2$: the attenuation vanishes and the ST-MLEE solution converges to the loss-free wave solution, recovering the classical limit.

4.1 Positive self-adjoint spectral-operator verification

We constructed the Dirichlet finite-difference Laplacian at $N = 24, 48, 96, 192$ and formed its spectral fractional power for $\beta = 1.6$. At $N = 192$ the relative symmetry defect was 1.50×10^{-16}, the minimum eigenvalue was positive (6.24), and the first fractional eigenvalue differed from its analytic sine-basis value by 1.77×10^{-5} (Figure 9). This verifies positivity, self-adjointness and spatial convergence for the stated spectral discretisation. This controlled check isolates the operator construction; the independent FEM and matched receiver-waveform tests below address discretisation independence and end-to-end accuracy.

4.2 Independent discretisation and evidence-closure checks

A consistent-mass linear FEM generalized eigenproblem, assembled independently of the finite-difference spectral matrix, converged at second order: the first fractional eigenvalue error decreased from 2.57×10^{-3} (16 elements) to 1.00×10^{-5} (256 elements). Three additional checks target the remaining discretisation objections (Figure 10). For the prescribed smooth periodic variable-β family, nested-grid operator-action differences decrease from 4.17×10^{-3} to 1.01×10^{-11}, and propagated-field differences decrease from 6.63×10^{-5} to 2.73×10^{-12}. This supports only the smooth declared family. On the 14,598-cell irregular grid, $m = 120$ and $m = 160$ errors relative to an extended $m = 240$ Lanczos reference are 1.445% and 0.237%. Finally, a non-shared two-dimensional classical-limit test compares discrete-sine modal evolution with direct leapfrog time marching on a separate 192^2 grid; the receiver difference decreases from 14.60% at 24^2 to 0.90% at 96^2. This last result applies only to $(\alpha, \beta) = (2, 2)$ and is an elastic-limit diagnostic, not a third-party fractional-wave validation.

4.3 Complete 2-D and small 3-D matched-accuracy wavefield benchmark

We next benchmark complete receiver waveforms rather than scalar temporal kernels. All methods use the same Dirichlet finite-difference Laplacian, smooth initial wavefield, three receivers, 24 output times on $[0, 0.55]$, and $(\alpha, \beta) = (1.72, 1.80)$. The two grids contain 64^2 and 26^3 unknowns. The 26^3 case is a small three-dimensional verification grid for matched-accuracy accounting, not a production 3-D seismic survey. ST-MLEE evaluates the modal Mittag–Leffler evolution directly; the independent controls are the velocity-form L1 method and a Caputo-corrected Grunwald–Letnikov (GL) history method at three time steps. Each timing is the median of three runs on an Intel64 Family 6 Model 183 CPU; the installed RTX 5070 was not used. Incremental peak resident memory was sampled at 2 ms. The spectral route has Krylov dimension zero and scalar Mittag–Leffler tolerance 10^{-12}; the history methods use direct diagonal modal solves.

Both history methods converge under step halving. At the prespecified 1.5% receiver waveform-error gate, the 2-D L1 and GL runs require $\Delta t = 0.00275$, take 0.15 s, and add

Table 5: Independent same-equation validation ledger for the complete-wavefield gate. All rows use the same fractional equation and the same self-adjoint Dirichlet operator as the ST–MLEE run being tested.

Test	Equation and operator	Independent part	Error metric	Pass gate
2-D receiver waveforms	$(\alpha, \beta) = (1.72, 1.80)$ on 64^2 Dirichlet grid	Velocity-form L1 and Caputo-corrected GL histories	Three-receiver waveform discrepancy at 24 output times	Both history controls below 1.5% at the matched step.
3-D receiver waveforms	Same fractional equation on 26^3 Dirichlet grid	Independently coded L1/GL time histories	Same receiver waveform metric and output schedule	Both history controls below 1.5%; ST–MLEE stores no time-history array.
Classical limit	$(\alpha, \beta) = (2, 2)$ on a separate sine-grid sequence	Direct leapfrog time marching	Receiver discrepancy under grid refinement	Reaches 0.90% at 96^2 versus 192^2; used only as an elastic-limit check.

approximately 6.3 MiB of resident memory, while ST-MLEE takes 0.15 s and adds less than 0.6 MiB. In 3-D, the matched L1 and GL runs take 0.24–0.25 s and add 26.8–26.9 MiB; ST-MLEE takes 0.22 s with no time-history array. The nested local $\beta = 2$ control is faster but has 20.5% and 34.5% waveform error and therefore does not enter the matched-accuracy ranking. Figure 11 reports the full runtime–error and memory comparison. This closes the complete-wavefield 2-D/3-D gate for the stated self-adjoint grids; it is not a heterogeneous production survey or GPU scalability claim.

Thus the primary validation does not rely on cross-model agreement: ST–MLEE, L1 and GL solve the same semidiscrete fractional equation, and the comparison isolates the requested-time evaluator rather than changes in the physical model.

4.4 Irregular heterogeneous sparse-operator Krylov gate

The preceding matched benchmark uses an analytic sine basis and therefore does not test the production route stated in the solver hierarchy. We next form the symmetric positive five-point operator $-\nabla \cdot (c^2 \nabla) + 0.02I$ on an irregular active-cell domain with a wavy top boundary, a Dirichlet notch, smooth layering, a high-velocity dome and a low-velocity dipping fault zone. A single-source matrix Mittag–Leffler action is approximated by Lanczos projection; the projected tridiagonal matrix is diagonalised once and reused at 13 output times and four receivers for that same starting vector. This tests a genuinely sparse numerical eigenaction rather than a full eigendecomposition, but it does not demonstrate multi-source Lanczos reuse.

Four grids from 32^2 to 128^2 contain 915, 3,648, 8,211 and 14,598 active cells. For each grid, Krylov dimensions 40, 80, 120 and 160 are nested in the same Lanczos run, and the $m = 160$ receiver traces provide the original internal projection reference. At $m = 120$ the relative receiver-waveform errors are 8.3×10^{-8}, 6.5×10^{-6}, 0.593% and 1.466%, respectively, so every grid passes the prespecified 1.5% gate. On the largest grid the measured CPU build-plus-evaluation time is 0.12 s and the explicitly stored sparse operator plus Krylov basis is 14.4 MiB (Figure 12). These numbers are route-diagnostic and scaling measurements on one CPU. The extended $m = 240$ calculation in Figure 10 checks the original projection truncation level within the same algorithm; it is not an exact PDE solution or a different solver. Non-self-adjoint PML, multi-source block Krylov, GPU kernels and field-scale meshes remain outside the claim. Standard PML and complex stretched-coordinate absorbing boundaries are generally non-self-adjoint and fall outside the real orthogonal modal diagonalisation proof. Extending the framework to those operators would require contour-integral or rational Krylov evaluations of matrix functions for sectorial, possibly non-normal matrices rather than the self-adjoint modal expansion used here. For this reason the section is called a sparse-operator *gate*, not a field-scale benchmark: it tests whether the fixed-operator matrix-function route survives an irregular positive operator and whether the projected result is stable against a larger Lanczos reference. It does not price communication, preconditioning, load balancing, or multi-source recycling.

Boundary handling in the validation contract. The main validation grids use the stated symmetric positive semidiscrete operators, so the modal theorem and the matched L1/GL controls refer to the same self-adjoint object. The sponge layers used in the auxiliary effective-medium controls are not part of that theorem. They are localized boundary-strip damping perturbations introduced only to suppress late boundary reflections in diagnostic wavefield runs, while the positive claims about history-free diagonalisation are made for the symmetric positive semidiscrete operator. Any production absorbing boundary that enters the operator itself, including standard PML or complex stretched-coordinate layers, must be treated as a non-self-adjoint extension rather than as evidence covered by the present proof.

For the largest tested grid, $m = 120$ is the economical screening choice because it meets the prespecified 1.5% waveform gate, whereas $m = 160$ is the preferred reporting choice when a discrepancy below 0.25% relative to the extended $m = 240$ calculation is required. These values are not universal. On a new operator, m should be increased until both consecutive projected receiver traces and a higher-dimensional reference satisfy the application tolerance; the reported memory and timing should then be charged at that selected dimension.

Scalar temporal-kernel cost context. After the complete matched-waveform gate, Figure 3 provides a narrower temporal-kernel comparison against a convergent $L1$ finite-difference discretisation of (2). On the analytic- eigenbasis problem used there, ST-MLEE attains the reference tolerance at lower temporal cost and without stored history, with the gap widening as the $L1$ scheme pays its $O(N_t^2)$ history convolution. This is supporting kernel-level cost evidence, not an end-to-end solver ranking; the complete 2-D/3-D comparison above supplies the matched- waveform claim for the stated semidiscrete grids.

4.5 Application-centred evidence boundary

The relevant test of ST-MLEE is predictive accuracy and cost at matched accuracy, not the mere availability of a closed formula. We therefore distinguish analytic or manufactured geometries, where spatial and temporal errors can be separated, from heterogeneous models, where the spatial operator is numerical. In the latter case "exact" means exact-in-time evaluation of the stated semidiscrete problem. A self-adjoint claim is made only for the spectral fractional Laplacian or an operator generated by a symmetric positive form. The method becomes geophysically useful only if later complex-model and cross-physics tests show lower phase/amplitude error, lower memory or runtime, or less biased inversion than an appropriate local constant-Q baseline.

Heterogeneous models. For a heterogeneous *velocity* $c(\mathbf{x})$ the spatial operator remains self-adjoint (e.g. $\mathcal{A} = -\nabla \cdot (c^2 \nabla)$), so it retains a discrete orthonormal eigenbasis and the ST-MLEE diagonalisation is preserved—one simply replaces the analytic (sine/Fourier) eigenpairs by the *numerical* eigenpairs of $\mathcal{A}$, and the history-free modal evaluation goes through unchanged. A spatially varying *order* is different in kind and is treated separately in §5; the same heterogeneous-velocity eigenbasis mechanism recurs there in the real-data forward of the Supplementary Material. Figure 13 propagates through a salt-dome velocity model (using the numerical eigenbasis of the heterogeneous operator), showing a stable, physically reasonable attenuated, dispersive wavefield; this single structurally realistic model is a deliberately *qualitative* illustration of stability and physical plausibility, not an additional quantitative accuracy benchmark. The quantitative same-equation validation of ST-MLEE against known behaviour and against an independent finite-difference scheme is given in Figures 3–6 (constant-Q flatness, dispersion exponent recovery, the classical-limit degeneration, and the accuracy/cost benchmark against the $L1$ scheme).

4.6 Effective-medium origin

To relate (1) to explicit heterogeneity, we propagate a full elastic wavefield through explicit fractal (von Kármán) random media with *no intrinsic loss*. Figure 14: elastic scattering alone produces an effective medium that attenuates, with the apparent attenuation *strength* controlled by the fractal statistics of the medium. Full-wave calibration tests show that the effective attenuation $1/Q$ varies systematically with the fractal dimension D_f, supporting reading the fractional orders as *physical*, heterogeneity-controlled quantities rather than free exponents. The same calibration also directly tests the popular closure $\beta = 3 - D_f$: in 1-D first-arrival transmission the velocity-dispersion signal is below measurability and the effective β remains close to the classical value; in 2-D acoustic scattering it departs only weakly from 2, far from the $\beta = H$ value the closure would require. The closure $\beta = 3 - D_f$ is therefore *not supported* by our full-wave calibration in transmission and near-source scattering geometries, and we do not adopt it here; β is treated as an empirically inverted parameter anchored qualitatively to medium heterogeneity and to the frequency dependence of $Q(\omega)$. Consistent with the conservative nature of $(-\Delta)^{\beta/2}$, the α/β division of labour is: the intrinsic-loss time order α is the carrier of energy dissipation (and absorbs the effective constant-Q fit of scattering attenuation), while β controls spatial non-locality and modulates both the attenuation angle and velocity dispersion through the βth-root wavenumber relation. Independent broadband amplitude-decay and phase-dispersion measurements are therefore needed to separate the two orders.

Sponge-boundary control. To confirm that the apparent attenuation in the fractal-medium experiments is due to scattering rather than absorbing boundary artefacts, a control run propagates the same source through a *homogeneous* medium (same geometry, same sponge layers). The control produces only negligible amplitude variation over the estimation aperture compared with the fractal runs, establishing that the measured effective Q is dominated by scattering, not by sponge absorption.

5 Prescribed variable-space-order semidiscrete operator

The fixed-operator argument extends to a prescribed spatially varying order $\beta(\mathbf{x})$ only after a concrete semidiscrete operator has been defined. For constant α, a real symmetric non-negative matrix has its own orthonormal eigenbasis, so its temporal evolution remains modal and history-free. This statement concerns the specified matrix, not a unique continuous variable-order fractional Laplacian. The companion WKB manuscript (Hu et al., 2026) instead analyses a continuous microlocal realization; sharing a frozen principal symbol does not make the two operators numerically or analytically interchangeable. The evidence below is explicitly restricted to smooth order profiles and to the prescribed projected matrix. Discontinuous geological interfaces are outside the positive claim unless an additional regularization or nonlocal transmission construction is supplied. The numerical audits therefore report the positive-semidefinite projection explicitly and include both a smooth nested-grid case and a discontinuous-order counterexample.

5.1 Variable space order $\beta(\mathbf{x})$: time-continuous modal evaluation of a prescribed semidiscrete operator

When only the space order varies (constant α), the time dependence can be represented without time discretisation after the spatial operator has been fixed. We prescribe $S_h[\beta] = \frac{1}{2}\{A_h[\beta] + A_h[\beta]^*\}$, where $A_h[\beta]$ is the discrete Kohn–Nirenberg quantisation of the grid symbol $c^2|\xi|^{\beta(\mathbf{x})}$ under the bounded-domain convention used in the code. This construction makes S_h real symmetric and reproduces the discrete Fourier multiplier for constant β; symmetry alone does not prove positivity or convergence to a unique continuous variable-order operator. The unprojected symmetrisation is not non-negative: the reproducible audit finds one eigenvalue of -2.1334×10^{-3} at each of $N = 24, 48, 96$ for the stated smooth contrast test. We therefore define the stable semidiscrete operator explicitly as the spectral projection $L_h = S_h^+ = \Psi \max(\Lambda, 0)\Psi^*$; this is a modelling definition, not round-off clipping. All claims below concern this prescribed projected realisation. Continuous-domain non-negativity and consistency remain open. Let (ν_n, ψ_n) be its numerical eigenpairs. Projecting ${}^{C}D_t^{\alpha}u + Lu = 0$ onto ψ_n gives, per mode, a constant-order scalar Caputo equation, so

$$u(\mathbf{x}, t) = \sum_n \langle u_0, \psi_n\rangle\, E_\alpha(-\nu_n t^\alpha)\, \psi_n(\mathbf{x}), \tag{14}$$

which is (10) with the numerical eigenbasis of L in place of the Laplacian eigenbasis: time-continuous at the semidiscrete level, history-free, and subject to no perturbative restriction on the amplitude of the β-variation. Figure 15 verifies this. Against an independently implemented constant-α $L1$ time-marching of the same operator L, the time-continuous modal ST-MLEE evaluation (14) reproduces the field to the reference's time-discretisation floor *independently of the β-contrast*, holding at $\beta(\mathbf{x}) \in [0.76, 1.98]$ (a full-range variation); for reference we also plot a naive weak-variation (perturbative) approximation, whose error grows with the contrast as expected. Refining the reference time step drives the $L1$ solution toward (14), confirming that the modal Mittag-Leffler evaluation is the time-continuous limit of the prescribed semidiscrete system. This comparison validates temporal evaluation, not spatial convergence to a general continuous variable-order operator. Thus the space order may be taken fully variable and non-local within this prescribed smooth projected-matrix definition at no loss of the history-free property; A four-grid audit ($N = 24, 48, 96, 192$) clarifies the evidence boundary. For the smooth periodic order profile, the relative PSD correction decreases from 1.37×10^{-5} to 1.24×10^{-7} and the projected fields differ from the $N = 192$ field by at most 1.52×10^{-9} on the coarser nested grids. For a discontinuous step in β, however, the unprojected minimum eigenvalue grows in magnitude from -0.35 to -95.7, the relative PSD correction increases from 1.92×10^{-3} to 5.17×10^{-3}, and the field differences decrease only from 9.33% ($N = 24$) to 2.85% ($N = 96$). Hence the smooth test supports consistency of this discrete sequence for smooth data, whereas the step test does not support a general continuous–discrete consistency claim. A directional perturbation check of the projected map gives relative first-order remainders $0.0103, 0.0204, 0.0399, 0.0766$ and 0.1427 for contrasts $0.02, 0.04, 0.08, 0.16, 0.32$, respectively, consistent with a locally differentiable map but not a global perturbative approximation. These results are generated by `vo1_projected_refinement.py` and archived as CSV. The projection S_h^+ is therefore not an interface physics law. For discontinuous order jumps it may remove or alter interface-localized components of the symmetrized Kohn–Nirenberg matrix, and the present evidence does not support using this projected construction as a sharp geological-interface simulator without an additional regularization or transmission model. An independent periodic singular-integral quadrature, which does not reuse the Kohn–Nirenberg matrix, gives relative operator-action differences 0.459, 0.392 and 0.338 and propagated-field differences 0.311, 0.254 and 0.211 on $N = 32, 64, 128$. The differences decrease but do not establish a common limit at these resolutions. This negative cross-definition result shows that "variable-order fractional Laplacian' is definition-dependent and prevents using same-matrix agreement as continuous-operator validation. It is treated as a definition-sensitivity audit by `vo1_independent_integral_check.py`. For visual continuity with the companion WKB manuscript, Figure 16 also shows a shared smooth two-dimensional low-Q anomaly diagnostic generated with the corresponding Kohn–Nirenberg matrix family. It supplies a wavefield snapshot and windowed local-Q samples for a genuinely two-dimensional smooth order perturbation, but it is not used to prove the ST-MLEE reuse theorem: the present paper's claim remains the time-continuous modal evaluation of a prescribed fixed self-adjoint matrix. It is only the *time* order that requires the expansion of the next subsection.

5.2 Extensions separated from the main claim

Jointly variable temporal and spatial orders do not admit one fixed modal evolution because the pointwise temporal order does not commute with spatial projection. The corresponding Laplace–Talbot/Bromwich formulation, its synthetic tests, the Cranfield closed-loop illustration, and the relaxation-order superposition are provided in the supplementary material. They remain history-free in the sense of avoiding stored time histories, but they require independent contour-node solves or multiple modal responses and therefore do not share the cost or reuse contract established here.

5.3 Measured fixed-operator reuse crossover

The reuse claim was tested separately with cached modal weights and an independently implemented L1 history solver on the same 26×26 Dirichlet operator. The L1 step 7.5×10^{-4} stores 561 history states per source and yields mean receiver discrepancies of 0.17–0.78% across one to 16 smooth source queries. Including the 0.0198 s modal-weight setup, the cached spectral totals are 0.0200–0.0226 s, whereas the L1 totals grow from 0.0477 to 0.788 s (Figure 4); the spectral evaluator stores no preceding time states. These CPU timings isolate the fixed-operator repeated-query mechanism and include the modal-weight setup, but not a general eigendecomposition, GPU, absorbing boundary or production mesh. In this analytic-basis audit the measured setup is 0.0198 s and the one-source L1 total already exceeds the cached spectral total (0.0477 versus 0.0200 s), so (11) gives $q_* = 1$ for this favourable small problem. This value should not be transferred to a heterogeneous mesh without charging the new setup cost.

6 Discussion

What is established. For a prescribed positive self-adjoint semidiscrete operator, requested-time evaluation can be separated from time marching. Dense modal evaluation is useful when an eigendecomposition can be amortised across times, receivers and source weights; sparse Lanczos projection provides the tested source-dependent matrix-action route on an irregular grid. The matched same-equation receiver tests and the extended Krylov reference quantify accuracy in those regimes, while the memory comparison concerns the recorded time-history array rather than total solver memory.

Relation to prior work. The dispersion model belongs to the established fractional-attenuation literature (Chen & Holm, 2004; Treeby & Cox, 2010; Zhu & Carcione, 2014), and modal Mittag–Leffler evolution is classical (Mainardi, 2010; Bazhlekova, 2001). The contribution is therefore numerical and evidential: one fixed-operator workflow, explicit accounting of setup versus reuse, and cross-checks that expose rather than hide the operator boundary. Existing variable-order finite-difference and Fourier pseudospectral schemes (O et al., 2024; Zhang et al., 2026) address broader operator classes; the prescribed variable-β experiment here instead asks how far the same fixed self-adjoint modal logic can be carried. The companion continuous-operator analysis (Hu et al., 2026) supplies mathematical context for the branch-resolved two-order model but is not evidence for the accuracy or reuse of ST-MLEE.

Enabling role for complex fractional media. The practical novelty is that ST–MLEE changes what can be explored reproducibly under a declared operator contract. With direct Caputo stepping, each additional output time, parameter diagnostic or receiver query carries the burden of the preceding history. In the fixed-operator setting, the temporal history is replaced by a reusable modal or projected matrix-function representation. That is what makes the more complex fractional-PDE experiments in this manuscript scientifically useful rather than merely formal: prescribed spatial nonlocality, smooth variable-space-order matrices, local low-Q anomalies, and relaxation-spectrum diagnostics can be queried repeatedly and audited against independent controls. The gain is enabling rather than universal; it applies while the operator representation remains fixed and does not by itself create a field-scale inversion, PML or multi-source sparse solver.

Limitations. The projected variable-β matrix is a modelling definition, and S_h^+ should not be read as a physical law for sharp interfaces. Smooth nested-grid agreement supports the tested discrete sequence, whereas the discontinuous-order and independent-integral results do not establish convergence to a general continuous variable-order operator. The $\beta = 3 - D_f$ closure is not adopted: lossless scattering in the tested calibration leaves β_{eff} close to 2, so a constitutive mechanism for genuine $\beta \neq 2$ remains open. Dense eigendecomposition is not a field-scale algorithm, and the present sparse test does not cover non-self-adjoint absorbing layers, preconditioned contour solves, graphics-processing-unit scaling, production meshes, or operator-rebuilding FWI loops. The supplementary joint-order and relaxation-spectrum studies have distinct cost paths and should not be read as evidence for the main fixed-operator performance claim.

Why the open extensions do not alter the present conclusion. The missing field-scale, FWI, PML and multi-source studies would be necessary to claim a production solver. They are not necessary to establish the narrower result proved and tested here: for a declared fixed positive self-adjoint operator, modal or projected Mittag–Leffler evaluation gives the requested-time solution without storing the preceding Caputo history, and the accuracy is checked against same-equation history solvers or a higher-dimensional Krylov reference. This separation is why the paper reports q_*, source-vector dependence and boundary self-adjointness as part of the method, rather than as after-the-fact caveats.

Cross-model falsification audit (not validation). The constant-order $L1$/GL audits are independent time-discretisation implementations of the same fixed semidiscrete fractional evolution, and the refined-grid leapfrog comparison reaches 0.90% only in the classical $(\alpha, \beta) = (2, 2)$ limit. The supplementary k-Wave-python 0.6.2 calculation deliberately tests a different governing equation and is therefore not part of the validation ladder above. Its preregistered primary $(1.94, 2)$ run was unstable and remains archived as a failure. In the stable-domain sensitivity, two grids reproduce the attenuation exponent within the frozen tolerance but give phase-velocity exponents near $+0.038$, opposite in sign to the ST-MLEE target -0.141. This mixed result is retained as a falsification boundary; community third-party fractional-wave validation, beyond the same-equation independent L1/GL controls reported here, remains open.

7 Conclusions

This study establishes a limited but reproducible result: when the semidiscrete spatial operator is prescribed, positive, self-adjoint, and fixed, fractional temporal evolution can be evaluated at requested times by modal Mittag–Leffler functions without storing the preceding time history. Analytic and classical-limit tests, independent finite-element assembly, convergent time-discretisation controls, and matched 2-D/3-D receiver benchmarks verify the dense implementation at the stated scales. The largest irregular test contains 14,598 active cells; relative to an extended 240-vector Lanczos reference, $m = 120$ differs by 1.445% and $m = 160$ by 0.237%. A separate classical-limit modal/leapfrog comparison reaches 0.90% at 96^2 versus 192^2.

For a prescribed smooth variable-space-order matrix, the nested-grid operator-action and propagated-field differences decrease to near round-off, but the discontinuous-order and cross-definition audits prevent a general continuous-operator claim. The practical conclusion is therefore conditional and complete within its stated contract: history-free requested-time evaluation is accurate and reusable for the tested fixed self-adjoint operators, with setup cost, source-vector dependence and boundary restrictions charged explicitly. Dense eigenbasis reuse and source-dependent Lanczos actions are deliberately separated throughout the paper. The k-Wave cross-model result is deliberately non-licensing because its attenuation agreement coexists with an opposite phase trend. The natural extensions are non-self-adjoint absorbing boundaries, block/recycling Krylov for multi-source sparse actions, and field-scale sparse performance; these are future production-solver questions rather than missing evidence for the fixed-operator method claim. Joint variable-time-order contour solves, the Cranfield closed-loop example, and relaxation-order superposition are retained in the supplement as separate extensions rather than as support for this conclusion.

Data Availability

Two published/public datasets are used. (i) The rock-physics motivation (Figure 2) replots the Table-1 median values of Sams et al. (1997) (doi:10.1190/1.1444249). (ii) The real-data demonstration (Supplementary Material) uses the public Denbury/LBNL Cranfield 3-D VSP (SECARB Phase III, well CFU 31F #1): raw true-amplitude SEG-Y shot records with geometry and the supplied first-break pick file; our scripts read the extracted near-offset shot (FFID 1219) and reproduce every processing step from the raw traces (windowing, spectra, spectral-ratio t^*, regularised $Q(z)$, $\alpha(z)$). All other results are synthetic. The reproducibility bundle `paper1_code_data_supplement.final.zip` supplied with this submission includes the constant-order ST-MLEE scripts `st_mlee_forward_1d.py`, `st_mlee_benchmark.py`, `st_mlee_modeling.py`, `st_mlee_layered_dispersion.py`, `st_mlee_saltdome.py`, `st_mlee_effective_medium.py`, and `p1_krylov_irregular_scaling.py`, and `p1_reuse_crossover_closure.py`; the independent cross-model script `p1_kwave_2d_crossmodel.py` with its preregistrations, CSV/JSON outputs, figure, and separate `requirements-kwave-lock.txt`; the exact variable-order scripts `vo1_beta_exact_stmlee.py` (variable $\beta(\mathbf{x})$ by the self-adjoint eigenbasis), `vo1_joint_talbot.py` (joint $\alpha(\mathbf{x}), \beta(\mathbf{x})$ by Laplace–Talbot), `vo1_wavefield_gallery.py` (the 1-D dual variable-order wavefield gallery), `vo1_wavefield_2d.py` (the 2-D circular-wavefront variable-Q demonstration), `vo1_sams_motivation.py` (Figure 2), `P1_2D_lowQ_anomaly.py` (the shared smooth 2-D low-Q anomaly diagnostic), and `vo1_cranfield_forward.py` (the real-VSP measurement and numerical forward of the Supplementary Material); the relaxation-spectrum script `do1_distributed_order.py`; and the auxiliary sponge-boundary control scripts `rp1_beta_calibration.py` and `rp1_sponge_control.py`. The submission package therefore includes the code and source data used for the reported validation, audit, and diagnostic outputs; the accepted version will additionally assign a persistent public repository DOI to the same review bundle. A container recipe or Code Ocean capsule can be supplied if required by the journal or repository. The scripts depend only on `numpy`, `scipy`, and `matplotlib`, and include the grid spacing, source frequency, velocity-fluctuation statistics, ensemble sizes, and random seeds used in the synthetic experiments. For double-anonymous review, the submitted review package includes an anonymized reproducibility archive with author-identifying paths removed, deterministic run commands, and machine-readable CSV/JSON outputs for every validation, audit, and diagnostic table or figure. Any public DOI archive will be created from that same review bundle rather than from an undocumented local working directory.

References

Aki, K., Richards, P.G., 1980. *Quantitative Seismology: Theory and Methods*. W.H. Freeman, San Francisco.

Abate, J., Valkó, P.P., 2004. Multi-precision Laplace transform inversion. *Int. J. Numer. Methods Eng.* **60**, 979–993, doi:10.1002/nme.995.

Bazhlekova, E., 2001. *Fractional Evolution Equations in Banach Spaces*. PhD thesis, Eindhoven University of Technology.

Blanch, J.O., Robertsson, J.O.A., Symes, W.W., 1995. Modeling of a constant Q: methodology and algorithm for an efficient and optimally inexpensive viscoelastic technique. *Geophysics* **60**, 176–184, doi:10.1190/1.1443744.

Caputo, M., Mainardi, F., 1971. Linear models of dissipation in anelastic solids. *La Rivista del Nuovo Cimento* **1**, 161–198, doi:10.1007/BF02820620.

Carcione, J.M., 2014. *Wave Fields in Real Media: Theory and Numerical Simulation of Wave Propagation in Anisotropic, Anelastic, Porous and Electromagnetic Media*, 3rd edn. Elsevier, Amsterdam.

Chen, W., Holm, S., 2004. Fractional Laplacian time–space models for linear and nonlinear lossy media exhibiting arbitrary frequency power-law dependency. *J. Acoust. Soc. Am.* **115**, 1424–1430, doi:10.1121/1.1646399.

Gorenflo, R., Kilbas, A.A., Mainardi, F., Rogosin, S.V., 2014. *Mittag-Leffler Functions, Related Topics and Applications*. Springer, Berlin, doi:10.1007/978-3-662-43930-2.

Higham, N.J., 2008. *Functions of Matrices: Theory and Computation*. SIAM, Philadelphia, doi:10.1137/1.9780898717778.

Hu, N., Li, S., Hu, C., Sun, J., 2026. Near-constant-Q seismic attenuation in variable-order fractional wave operators: branch-resolved WKB criteria. Separate manuscript in preparation.

Hochbruck, M., Lubich, C., 1997. On Krylov subspace approximations to the matrix exponential operator. *SIAM J. Numer. Anal.* **34**, 1911–1925, doi:10.1137/S0036142995280572.

Holm, S., Näsholm, S.P., 2011. A causal and fractional all-frequency wave equation for lossy media. *J. Acoust. Soc. Am.* **130**, 2195–2202, doi:10.1121/1.3631626.

Kjartansson, E., 1979. Constant-Q wave propagation and attenuation. *J. Geophys. Res. Solid Earth* **84**, 4737–4748, doi:10.1029/JB084iB09p04737.

Komatitsch, D., Martin, R., 2007. An unsplit convolutional perfectly matched layer improved at grazing incidence for the seismic wave equation. *Geophysics* **72**, SM155–SM167, doi:10.1190/1.2757586.

Kwaśnicki, M., 2017. Ten equivalent definitions of the fractional Laplace operator. *Fract. Calc. Appl. Anal.* **20**, 7–51, doi:10.1515/fca-2017-0002.

Lubich, C., 1986. Discretized fractional calculus. *SIAM J. Math. Anal.* **17**, 704–719, doi:10.1137/0517050.

Mainardi, F., 2010. *Fractional Calculus and Waves in Linear Viscoelasticity*. Imperial College Press, London, doi:10.1142/p614.

McDonal, F.J., Angona, F.A., Mills, R.L., Sengbush, R.L., Van Nostrand, R.G., White, J.E., 1958. Attenuation of shear and compressional waves in Pierre shale. *Geophysics* **23**, 421–439, doi:10.1190/1.1438489.

Mu, X., Huang, J., Wen, L., Zhuang, S., 2021. Modeling viscoacoustic wave propagation using a new spatial variable-order fractional Laplacian wave equation. *Geophysics* **86**, T487–T507, doi:10.1190/geo2020-0610.1.

Mu, X., Huang, J., Yang, J., Li, Z., Ivan, M.S., 2022. Viscoelastic wave propagation simulation using new spatial variable-order fractional Laplacians. *Bull. Seismol. Soc. Am.* **112**, 48–77, doi:10.1785/0120210099.

Müller, T.M., Gurevich, B., Lebedev, M., 2010. Seismic wave attenuation and dispersion resulting from wave-induced flow in porous rocks—a review. *Geophysics* **75**, 75A147–75A164, doi:10.1190/1.3463417.

Näsholm, S.P., Holm, S., 2013. On a fractional Zener elastic wave equation. *Fract. Calc. Appl. Anal.* **16**, 26–50, doi:10.2478/s13540-013-0003-1.

O'Doherty, R.F., Anstey, N.A., 1971. Reflections on amplitudes. *Geophys. Prospect.* **19**, 430–458, doi:10.1111/j.1365-2478.1971.tb00610.x.

Pride, S.R., Berryman, J.G., Harris, J.M., 2004. Seismic attenuation due to wave-induced flow. *J. Geophys. Res. Solid Earth* **109**, B01201, doi:10.1029/2003JB002639.

Robertsson, J.O.A., Blanch, J.O., Symes, W.W., 1994. Viscoelastic finite-difference modeling. *Geophysics* **59**, 1444–1456, doi:10.1190/1.1443701.

Sams, M.S., Neep, J.P., Worthington, M.H., King, M.S., 1997. The measurement of velocity dispersion and frequency-dependent intrinsic attenuation in sedimentary rocks. *Geophysics* **62**, 1456–1464, doi:10.1190/1.1444249.

Sato, H., Fehler, M.C., Maeda, T., 2012. *Seismic Wave Propagation and Scattering in the Heterogeneous Earth*, 2nd edn. Springer, Berlin, doi:10.1007/978-3-642-23029-5.

Shapiro, S.A., Hubral, P., 1999. *Elastic Waves in Random Media*. Springer, Berlin.

Talbot, A., 1979. The accurate numerical inversion of Laplace transforms. *J. Inst. Math. Appl.* **23**, 97–120, doi:10.1093/imamat/23.1.97.

Treeby, B.E., Cox, B.T., 2010. Modeling power law absorption and dispersion for acoustic propagation using the fractional Laplacian. *J. Acoust. Soc. Am.* **127**, 2741–2748, doi:10.1121/1.3377056.

Wang, Y., 2008. *Seismic Inverse Q Filtering*. Blackwell Publishing, Oxford.

Weideman, J.A.C., Trefethen, L.N., 2007. Parabolic and hyperbolic contours for computing the Bromwich integral. *Math. Comp.* **76**, 1341–1356, doi:10.1090/S0025-5718-07-01945-X.

Winkler, K.W., Nur, A., 1982. Seismic attenuation: effects of pore fluids and frictional-sliding. *Geophysics* **47**, 1–15, doi:10.1190/1.1441276.

Yuan, L., Agrawal, O.P., 2002. A numerical scheme for dynamic systems containing fractional derivatives. *J. Vib. Acoust.* **124**, 321–324, doi:10.1115/1.1448322.

Zhu, T., Carcione, J.M., 2014. Theory and modelling of constant-Q P- and S-waves using fractional spatial derivatives. *Geophys. J. Int.* **196**, 1787–1795, doi:10.1093/gji/ggt483.

O, C.W., Ro, W.M., Kim, Y.C., 2024. An explicit finite difference approximation for space-time Riesz–Caputo variable order fractional wave equation using Hermitian interpolation. *Numer. Anal. Appl.* **17**, 262–275, doi:10.1134/S1995423924030054.

Zhang, Y., Zhao, X., Zhou, S., 2026. Fourier pseudospectral methods for the variable-order space fractional wave equations. *Comput. Phys. Commun.* **318**, 109876, doi:10.1016/j.cpc.2025.109876.

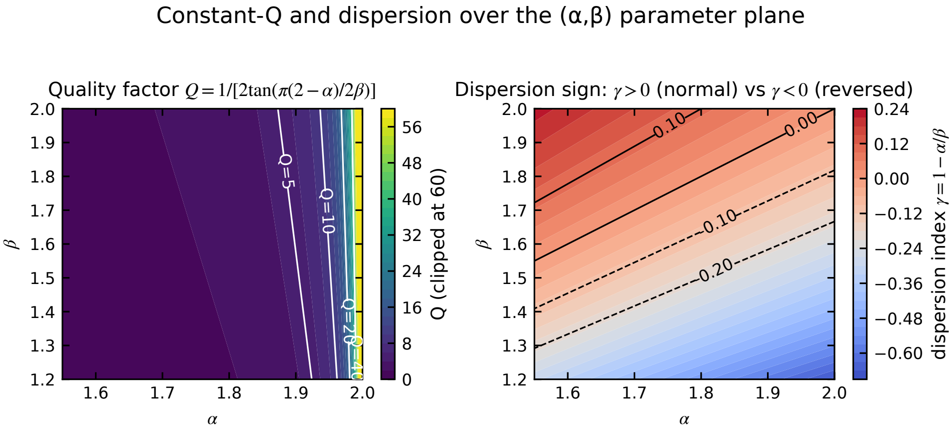

Figure 1: Order-to-observable map. The forward map $(\alpha, \beta) \mapsto (Q, \gamma)$ over the admissible range; the smooth, invertible correspondence used by order-recovery methods.

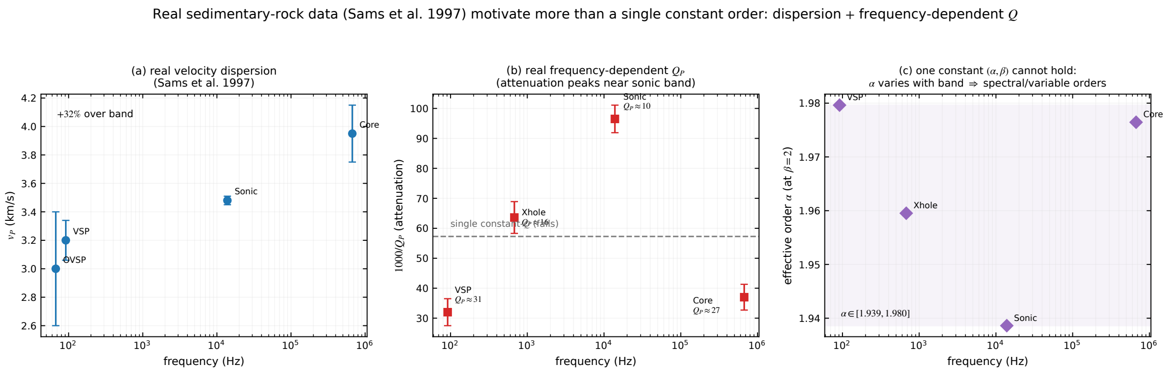

Figure 2: Measured, frequency-axis motivation: the sedimentary-rock dataset of Sams et al. (1997) (Table 1, intrinsic, scattering-corrected medians; error bars are standard errors), one location sampled at different frequencies. (a) Real P-velocity dispersion across the seismic-to-ultrasonic band ($\approx +30\%$): Q does not lock the dispersion to a single value, the empirical basis for admitting $\beta \neq 2$. (b) Real intrinsic attenuation $1000/Q_P$: strongly frequency dependent and peaked near the sonic band; no single constant-Q level (dashed) fits, motivating the relaxation-order spectrum $\rho(\alpha)$ of the Supplementary Material. (c) The effective time order obtained by mapping each band's Q through the $\beta = 2$ member varies from band to band—evidence against a single order *at one point in frequency*, not evidence of spatial variation. The panel motivates the supplementary relaxation-spectrum route; the main-text performance claim remains the fixed-operator constant-order or prescribed-matrix evaluation. Data replotted from Sams et al. (1997). Produced by `vo1_sams_motivation.py`.

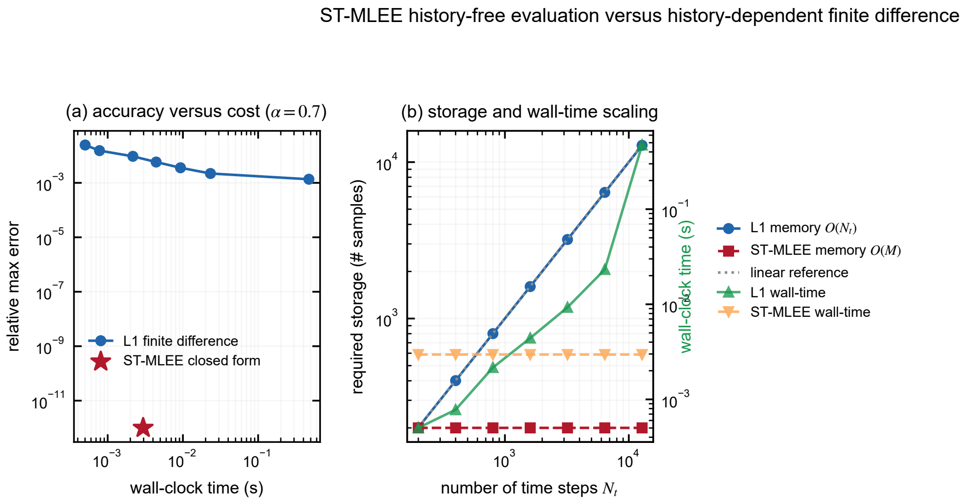

Figure 3: Accuracy/cost benchmark. ST-MLEE reaches reference accuracy against a convergent $L1$ finite-difference scheme while remaining history-free.

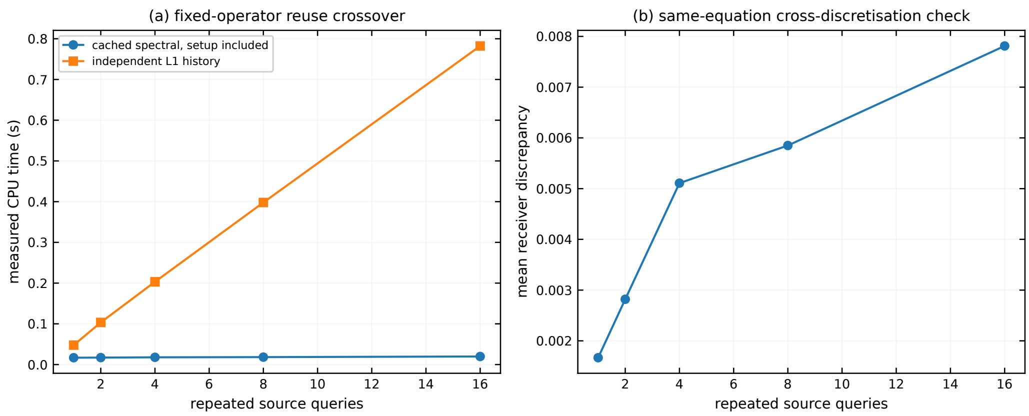

Figure 4: Fixed-operator reuse audit. (a) Measured CPU totals for cached spectral requested-time evaluation and an independent L1 history solver on the same Dirichlet operator. (b) Same-equation receiver discrepancy for the refined L1 control. The audit uses repeated fixed-operator queries; it is not evidence that a standard Lanczos basis can be reused after changing the source vector.

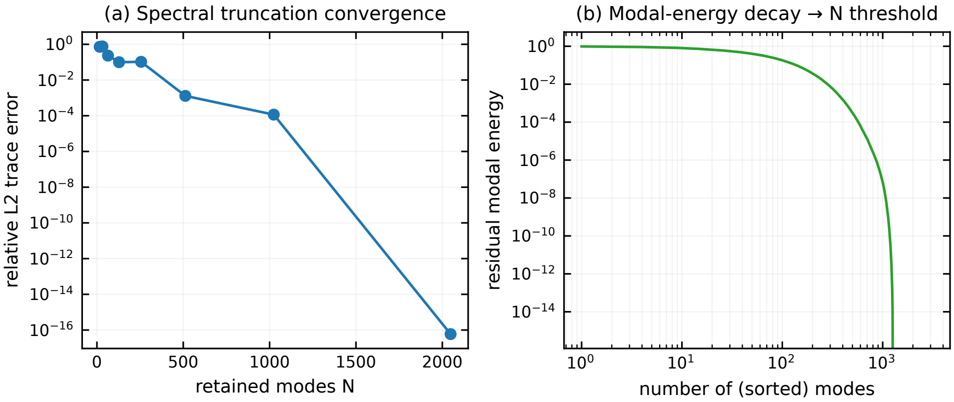

Figure 5: Modal truncation error. Relative error of the ST-MLEE series (10) versus the number of retained eigenmodes, controlling the spatial accuracy.

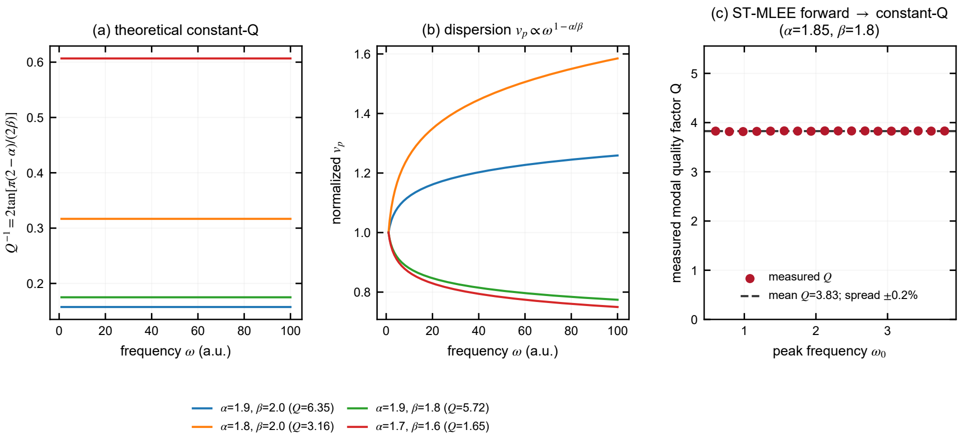

Figure 6: Constant-Q diagnostic. The medium reproduces a frequency-flat quality factor across the tested frequency band.

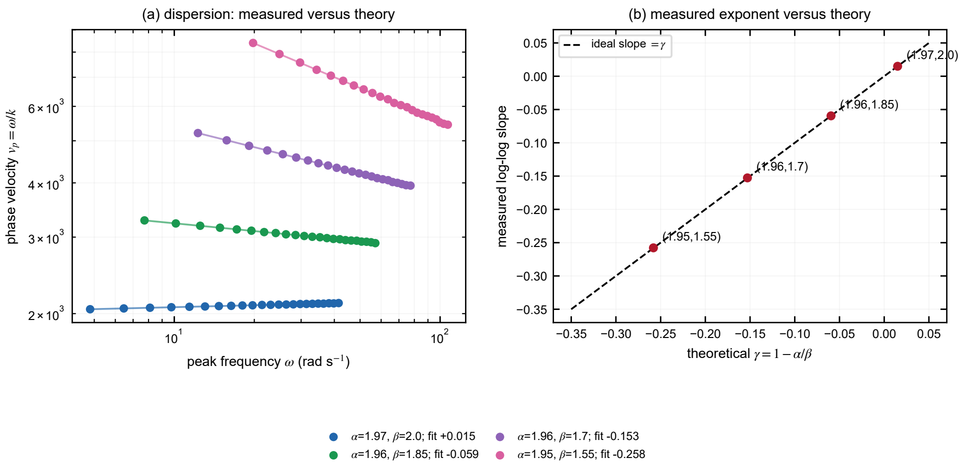

Figure 7: Velocity dispersion. The phase velocity follows $v_p \propto \omega^\gamma$ with $\gamma = 1 - \alpha/\beta$.

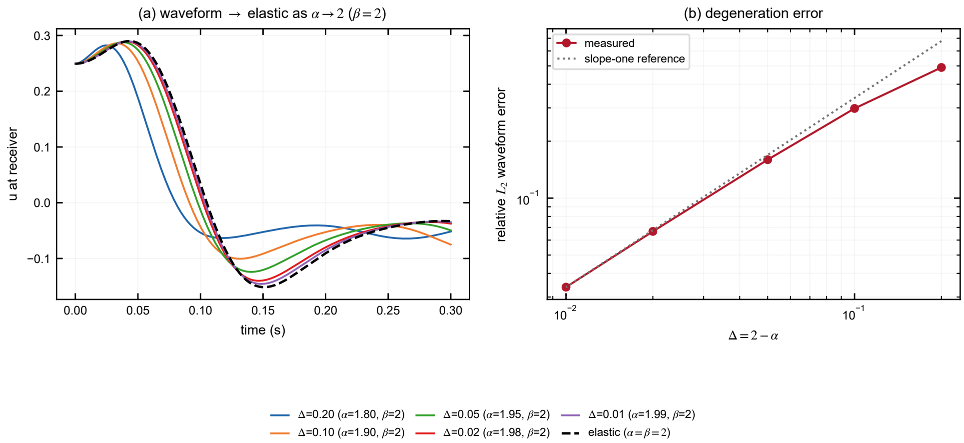

Figure 8: Classical (elastic) limit. As $\alpha \to 2$ at $\beta = 2$ the attenuation vanishes and ST-MLEE converges to the loss-free wave solution.

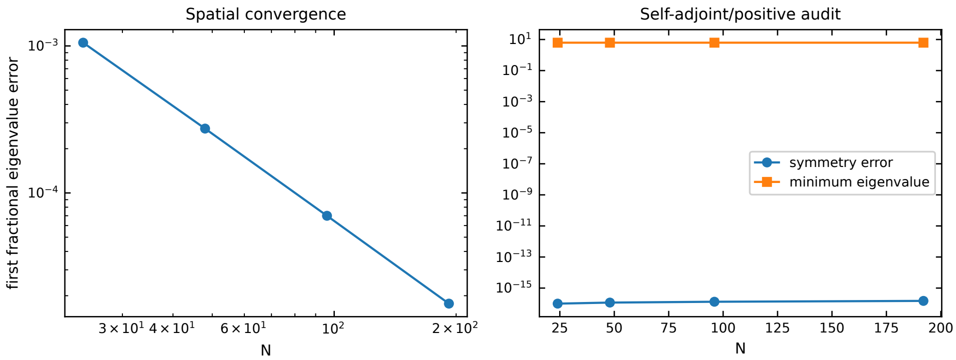

Figure 9: Positive self-adjoint operator verification: fractional eigenvalue convergence and symmetry/positive-spectrum audit.

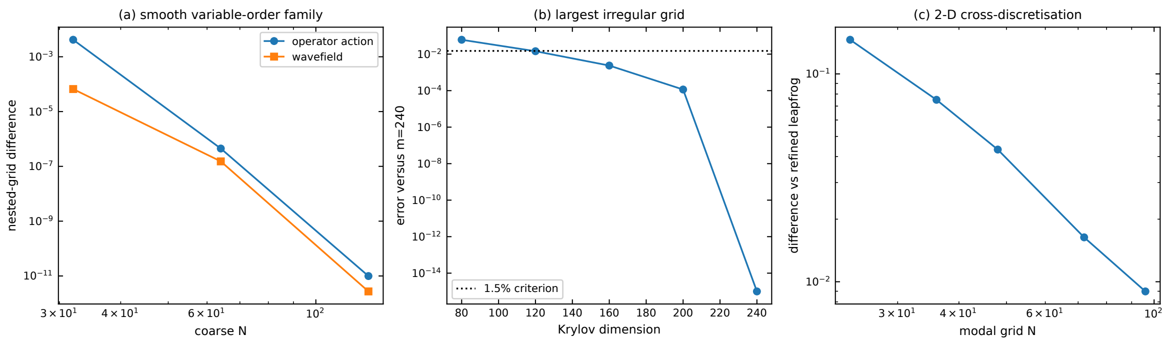

Figure 10: Evidence-closure checks. (a) Smooth variable-order nested-grid differences. (b) Largest-grid Lanczos convergence to $m = 240$. (c) Two-dimensional classical-limit modal versus separately refined leapfrog receiver comparison.

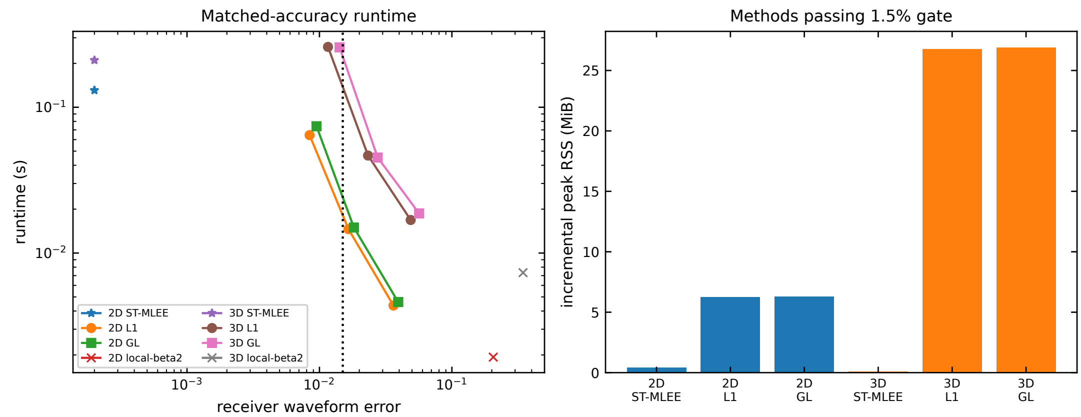

Figure 11: Complete-wavefield matched-accuracy benchmark. Left: runtime versus receiver waveform error. Right: incremental peak memory for methods passing the 1.5% gate.

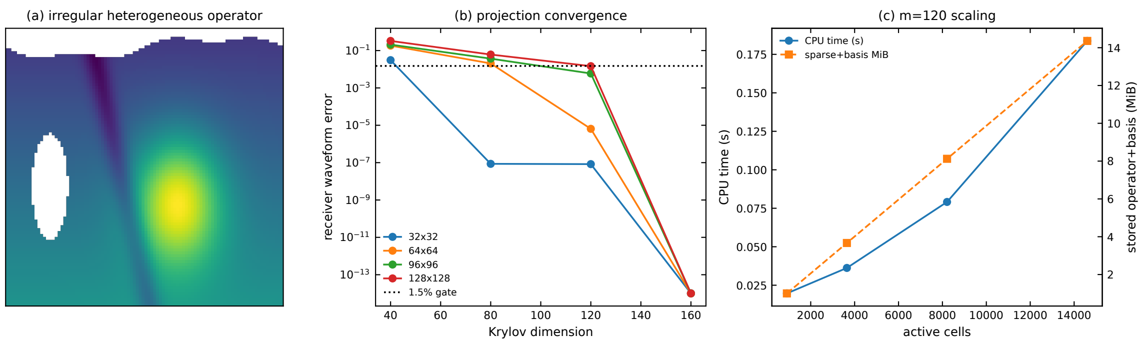

Figure 12: Irregular heterogeneous sparse-operator Krylov gate. (a) Representative active-cell coefficient field. (b) Receiver-waveform convergence to the nested $m = 160$ projection reference; $m = 120$ passes 1.5% on all four grids. (c) Measured CPU time and explicit sparse-operator-plus-basis storage at $m = 120$.

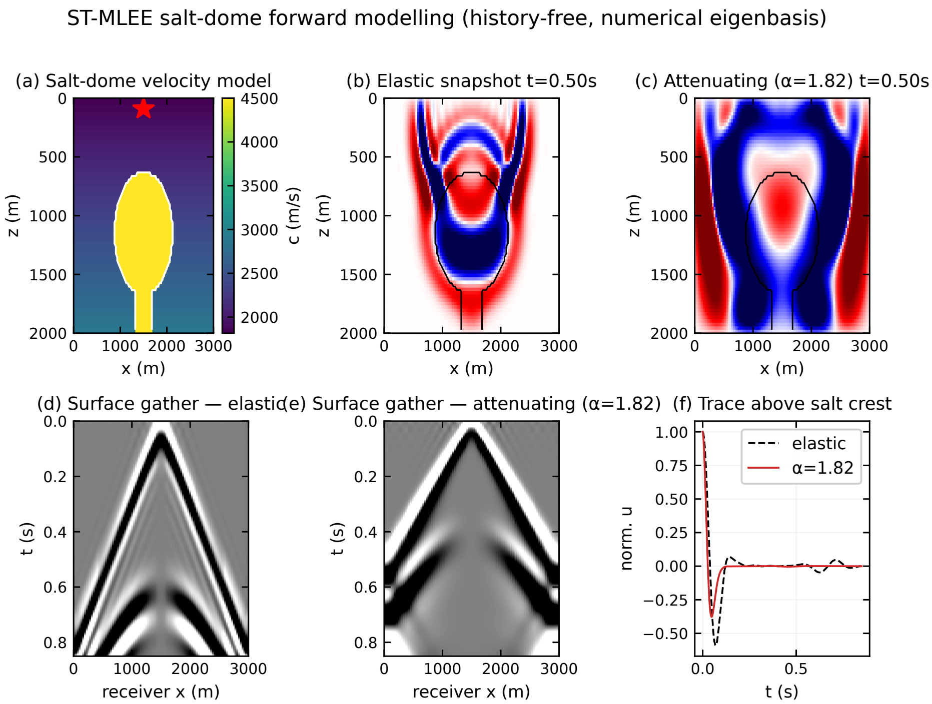

Figure 13: Salt-dome model. ST-MLEE propagation through a salt-dome velocity structure, using the numerical eigenbasis of the heterogeneous operator: a qualitative illustration of stability on a structurally realistic model.

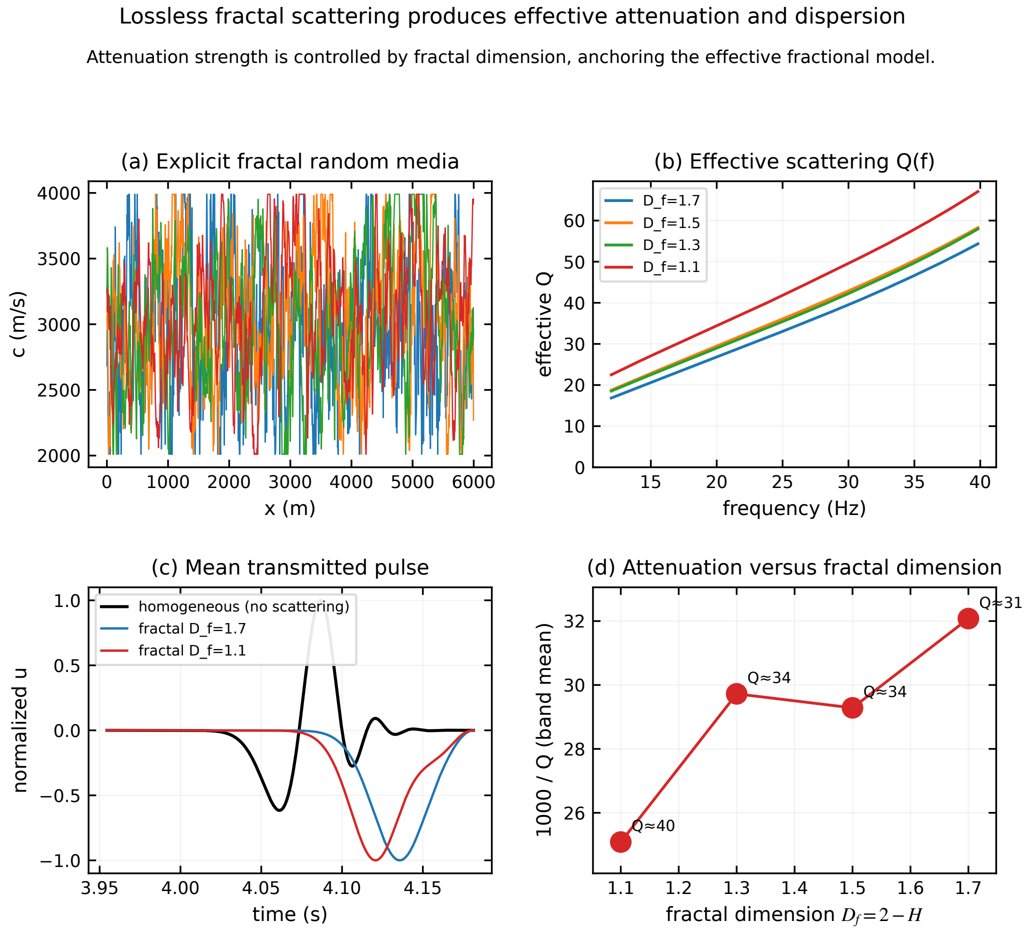

Figure 14: Effective-medium origin. Full elastic propagation through *lossless* fractal random media: scattering alone yields an effective attenuating, dispersive medium, anchoring the fractional equation physically.

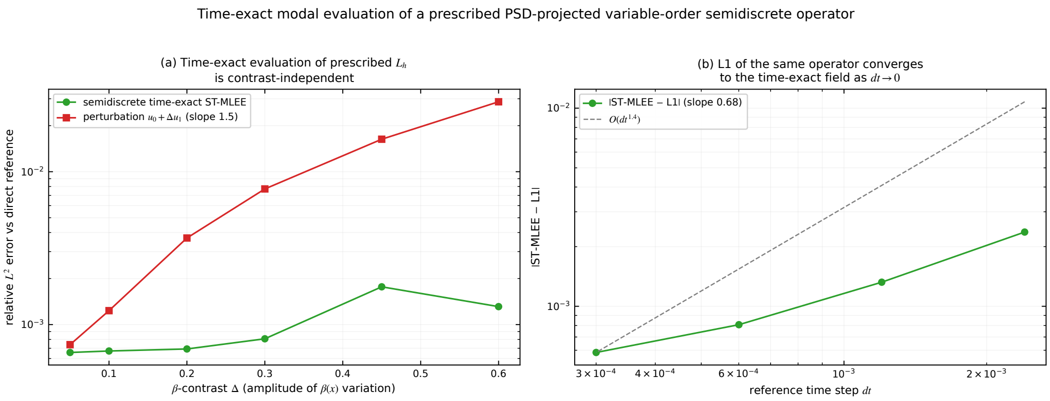

Figure 15: Time-exact modal evaluation of a prescribed PSD-projected variable-space-order semidiscrete operator by ST-MLEE (constant α). Here *time-exact* refers only to direct Mittag–Leffler evolution of the prescribed finite-dimensional operator, not to exactness or convergence of an underlying continuous variable-order operator. (a) Relative error versus β-contrast Δ: the semidiscrete time-exact ST-MLEE evaluation (14) on the eigenbasis of the self-adjoint variable-order operator stays at the reference floor for all contrasts, while a naive weak-variation (perturbative) approximation degrades as the contrast grows. (b) Refining the reference time step drives the independent $L1$ solution of the same operator toward the semidiscrete time-exact ST-MLEE field, confirming (14) is the time-continuous semidiscrete limit. Produced by `vo1_beta_exact_stmlee.py`.

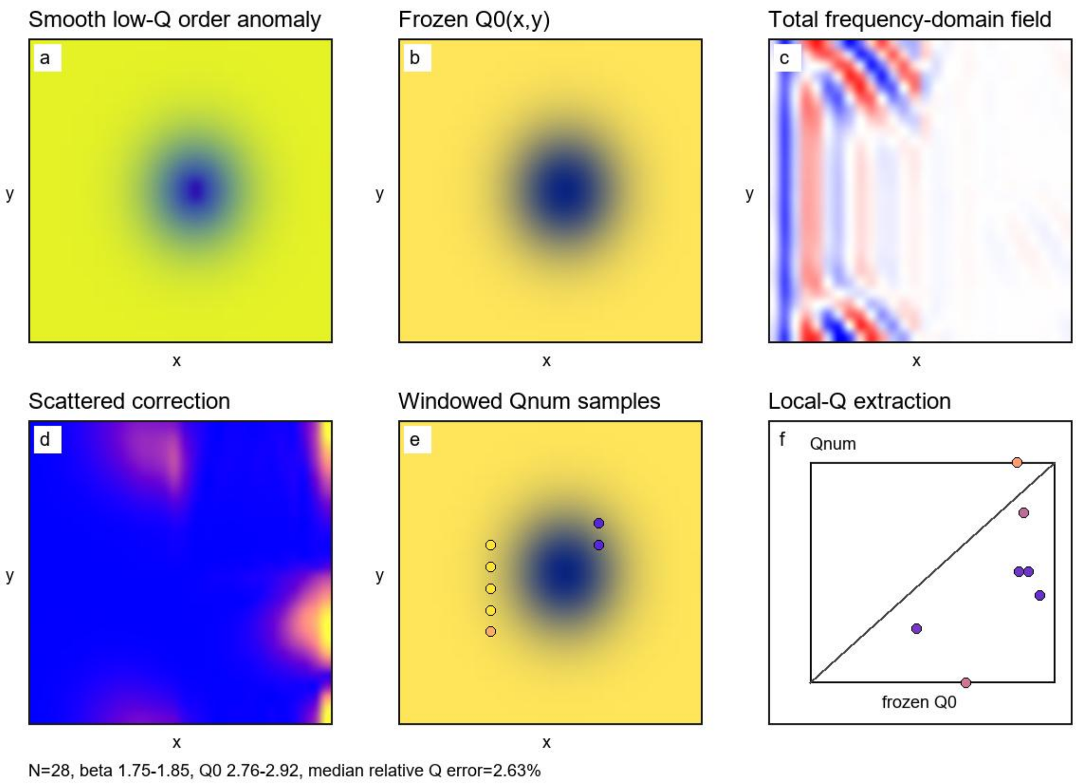

Figure 16: Smooth two-dimensional low-Q anomaly diagnostic. (a) Smooth nonseparable order anomaly. (b) Frozen branch quality-factor field $Q_0(x, y)$. (c) Total frequency-domain field. (d) Relative scattered correction. (e) Windowed local Q_{num} samples accepted by a local plane-wave residual gate. (f) Extracted Q_{num} against frozen Q_0 for the accepted windows. This is a finite-dimensional smooth-anomaly diagnostic and wavefield snapshot; it does not extend the fixed-self-adjoint ST-MLEE reuse claim to sharp interfaces or field-scale inversion.